

# Omnisoot: an object-oriented computational package for the simulation of the gas phase synthesis of carbonaceous nanoparticles

Mohammad Adib\*, Sina Kazemi<sup>1</sup>, M. Reza Khgolghy<sup>1, †</sup>

---

\*Department of Mechanical and Aerospace Engineering, Carleton University, 1125 Colonel By Dr, Ottawa, ON K1S 5B6, Canada

<sup>†</sup>Correspondeing author

# 1 Introduction

The formation of carbonaceous nanoparticles such as soot and Carbon Black (CB) is a complex and multi-scale process that involves chemical reactions, heat transfer, and fluid and particle dynamics and spans over wide length ( $\sim 10^{-12}$  to 1 m) and time ( $\sim 10^{-15}$  to 1 s) scales. Understanding the effect of process parameters on particle concentration, morphology, and composition is not trivial, but crucial in health and environmental impacts soot and functional properties of CB. Soot particles are broad-band light absorbers [1], and emitted in large scales ( $\approx 9.5$  megatons of soot) acting as the third strongest contributor to climate change after methane and carbon dioxide [2]. Because of their small size (classified as  $\text{PM}_{2.5}$ ), soot particles can deposit on lung tissues and penetrate other organs through the bloodstream [3] and cause asthma [4] and heart disease [5]. On the other hand, CB is the largest flame-made nanomaterial by production value and volume ( $\sim 15$  megatons per year with a worth of \$17B) extensively used as a reinforcing agent in rubber and tire industries [6], and conductive additive in lithium-ion batteries [7]. CB is primarily manufactured by the furnace process which suffers from low mass yield and excessive emission, generating 4 tons of  $\text{CO}_2$  per each ton of product on average [8]. Alternative technologies such as plasma-powered reactors for co-generation of hydrogen and CB from methane decomposition has drawn considerable interest [9, 10, 11] thanks to advantages over conventional methods in terms of yield and reduction of  $\text{CO}_2$  emission or other pollutants [12]. Controlling CB yield, structure, morphology and composition is crucial to produce specific grades of CB tailored for various applications in both conventional and new production methods. However, the effect of process parameters such as feedstock composition, pressure, and temperature-time-history on CB properties has not been completely understood yet due to complexities of gas chemistry and CB inception and surface growth. Therefore, there is a clear need for robust computational models to predict yield, particle structure and composition under different process conditions [13] and to reduce soot emission in combustion devices.

"soot" and "Carbon Black" are distinct materials in terms of chemical properties and synthesis process [14]. While soot usually refers to the unwanted particulate matter formed during incomplete combustion of any carbon-containing material with variable organic content and a large variation in C/H ratio [14], CB is commercially produced under highly controlled partial combustion or thermal decomposition of hydrocarbons. This work focuses on soot particles generated under controlled laboratory conditions from fuels with known compositions. The mature soot formed in methane and ethylene premixed flame can reach 95% elemental C/H ratio [15], which is close to CB composition. The comparison of transmission electron microscopy (TEM) images of industrially produced CB [16] with soot sampled from diesel fuel [17, 18] indicates similarity of their morphology and structure. Hereafter, soot will be used to collectively refer to carbonaceous nanoparticles produced in flame/reactor during combustion/pyrolysis processes.

The TEM analysis of soot sampled from flames [18], reactors [19], and engines [20] with different fuels and process conditions revealed a common fractal-like morphology, often characterized as agglomerates of primary particles. High resolution transmission electron microscopy (HRTEM) of soot primary particles showed clusters of precondensed Polycyclic Aromatic Hydrocarbons (PAHs) [21] pointing to PAH as main soot precursors. This hypothesis was also supported by thermodynamic stability of PAHs enabling them to resist dissociation at high flame temperatures [22].

However, the transition PAHs (soot precursors) to incipient soot, known as *soot inception* has not been well understood at the level of pathways and elementary reactions [23] primarily due to uncertainties in PAH (precursor) chemistry, and the kinetics of PAH growth into soot particles, which is highly reversible hence sensitive to local temperature, pressure and intermediate species concentration [23].

It is not clear how PAH clusters form and what forces allow the binding occur and resist dissociation at flames temperatures ( $\geq 1600$  T). Frenklach [24] characterized the clustering as a physical process where the sticking of PAHs upon collision forms dimers held together by Van der Waals (vdW) forces without involving chemical reactions. In fact, Herdman and Miller [25] found that the binding energy of PAHs dimers due to dispersive and electrostatic forces increases linearly with molecular mass and reaches the limit of exfoliation energy for graphite. However, the entropy barrier of dimerization increases with PAH size making them unfavorable under equilibrium conditions. So,

PAHs as large as circumcoronene ( $C_{54}H_{18}$ ) can only form dimer to survive flame temperatures [23]. However, the concentration of large PAHs are too low to account for the observed number density of soot particles in flames [26].

Despite the gaps in fundamental understanding of soot formation and limitations of diagnostics methods, models have been developed describe the soot inception and growth. These models have been formulated as a set of clear pathways that explain soot inception based on collisions of PAH molecules. They have to be consistent with current knowledge of soot physics, feasible to be coupled with chemistry and particle dynamics models, and able to predict soot mass, PSD and morphology observed in flames and reactors.

The classic description of soot inception relies on PAH dimerization where collision of two PAH molecules (monomers in this context) forms a dimer held together by Van der Waals forces [27]. The dimerization is a irreversible process with an efficiency that accounts for the reversibility or dissociation of dimers. The theory postulates that PAH growth continues by sequential addition of a monomer (PAH molecule) forming stacks of dimers, trimers, tetramers and so on to reach a certain mass threshold that marks the emergence of incipient soot [27], but for practical purposes, a dimer is usually considered as incipient soot. Here, we call this model *Irreversible Dimerization*. Irreversible Dimerization has been used to predict soot formation in burner-stabilized premixed [28, 29], counterflow diffusion flames [30, 31], coflow diffusion flames [32, 33]. A collision efficiency factor ranging between  $10^{-6}$  to 1 is also employed to adjust the inception flux and PAH adsorption rates to achieve desired soot mass and size distribution. PAHs of moderate sizes such as pyrene (4 rings) to coronene (7 rings) have been considered as the starting point of inception due to their thermodynamic instability that justifies the irreversibility at high temperatures [27]. However, the theoretical calculations [34] and experiments [35] indicated that PAH dimerization is highly reversible in flame conditions.

The inception flux of irreversible dimerization is mainly controlled by PAH concentration due to weak temperature dependence, so it produces new particles at low temperatures (even less than 500 K) [36] despite experimental evidence for termination of inception below 1200 K [37, 38]. Also, the arbitrary selection of efficiency factors alters the distribution of mass between inception of surface growth the could significantly change soot mass, PSD, and morphology [39]. Miller [40] used equilibrium constant for PAH dimerization to calculate the net dimerization rate and demonstrated that the collision of PAHs larger than circumovalene ( $\sim 800$  amu) could last long enough grow into incipient soot. However, the concentration of PAHs drops rapidly with size [23]. The entropy barrier of dimerization is significant for larger PAHs [41].

Eaves et al. [42] relaxed the irreversibility assumption, and developed a reversible clustering model to simulate inception using an array of PAHs from naphthalene to benzo-pyrene. Building on that work, Kholghy et al. [43] emphasized on the necessity of chemical bond formation after physical PAH clustering for accurate prediction of volume fraction, primary particle diameter and PSD in ethylene coflow diffusion flames. Later, Kholghy et al. [44] proposed the *"Reactive Dimerization"* model which starts with reversible collision of PAHs leading to physical dimers held with vdW forces that are graphitized and form chemically-bonded dimers that serve as soot nuclei grow via surface reactions. They also performed a systematic analysis on the contribution of different PAHs, and concluded that one- and two-ring aromatics account for almost all of inception flux in the so-called *"sooting flame"* [29]. However, Frenklach and Mebel [45] pointed out that an inception model that initiated with a highly reversible step similar to Reactive Dimerization [44] cannot produce sufficient flux of particles to match measurements of the benchmark burner-stabilized stagnation flame [46]. Instead, they proposed a HACA-driven mechanism where addition of monomer molecule to its radical activated by hydrogen abstraction for a stable dimer via an E-Bridge bond formation, and this sequential process continues to form trimers, tetramers, and larger PAH clusters.

The gas-phase chemistry of aromatics can be extended to account for chemical growth of incipient soot via surface reactions [24]. This hypothesis, known as "chemical similarity" postulates that the reactions occurring on the soot surface are similar to those involving large molecules of PAHs in the gas phase. It also provides means to describe the rates of surface growth and particle oxidation in terms of elementary chemical reactions. In other words, it is assumed that the surface of soot particles is made up of lateral faces of larges PAHs covered with C-H bonds. This is the basis

for HACA mechanism [27, 47] that assumes the soot surface to consist of hydrogenated sites with a predefined density. Mass growth on soot surface requires H-abstraction to form a radical site, followed by acetylene attack similar to growth of PAH molecules in the gas-phase. The reactivity of these sites changes with time and temperature [48, 49], described as soot aging. For modelling purposes, a temperature-dependent multiplier, usually represented by  $\alpha$ , was introduced to account for these effects. Appel et al. [47] showed  $\alpha$  changes with temperature and particle size.

Adsorption of PAHs on the surface of soot particles is also a viable growth mechanism [27], more specifically called physisorption or chemisorption depending on the mechanisms driving the adsorption process [50]. There is still debate over the stability of adsorbed PAH molecules on soot surface [51]. Following the hypothesis that PAHs are building blocks of soot particles, a mechanism similar to inception is often used to describe PAH-soot growth.

In typical soot formation processes such as flames and reactor, soot particles are formed at high concentrations ( $10^{12}$  1/cm<sup>3</sup>), and inception and surface growth are relatively short compared to the total residence of soot particles. As a result, coagulation becomes dominant rapidly attaining both [52] self-preserving size distribution (SPSD) [53] and asymptotic fractal-like structure [54]. The evolving fractal-like structure of agglomerates quantified by their mobility diameter normalized by primary particle,  $d_m/d_p$ , and gyration,  $d_m/d_g$ , diameters can be described with power laws derived from mesoscale simulations [55]. The collision frequency of agglomerates depends on their evolving fractal-like morphology. Also, polydisperse agglomerates collide more frequently than monodisperse ones. The enhancement in their collision frequency reaches an asymptotic value of 35% [52] or 82% [56] in the free molecular or transition regimes, respectively at SPSPD regardless of the polydispersity in their constituent primary particles. Particle morphology formed by inception, surface growth and agglomeration can be tracked precisely by mesoscale simulations, such as Discrete Element Modeling (DEM) [57]. However, they are computationally expensive and interfacing them with chemical kinetics in computational fluid dynamics (CFD) simulations is not trivial [58]. This limits their application. So, sectional population balance models (SPBM) are often used to track agglomerate and primary particle size distribution [59], morphology [60], and composition [32] in complex laminar [32] and turbulent flows [61]. Using the SPBMs coupled with relations for agglomerate fractal-like structure [62] and collision frequency [63], particle size distribution, morphology and composition can be tracked accurately. However, the computational cost of SPBMs increases exponentially with the number of sections [64] and particle properties [32] tracked. Thus, one property (e.g. agglomerate mass) is typically tracked with SPBMs to reduce computational cost. This does not allow to account for agglomerate fractal-like structure [65, 66] which limits SPBM accuracy in predicting surface growth and coagulation rate of agglomerates and their size distribution.

Alternatively, particle dynamics can be tracked by the method of moments (MOM) [67] or monodisperse population balance models (MPBM) [68]. Such models only track average particle properties (e.g. moment ratios) and their accuracy could be limited if unrealistic assumptions (e.g. approximating agglomerates as monodisperse and perfect spheres) are used. However, when inception and surface growth are short [69] and high particle (number) concentrations are formed [55], they lead to rapid attainment of self-preserving size distributions (SPSD) and agglomerates having asymptotic structure [52]. In this case a MPBM or MOM can be assembled on a firm scientific basis with accuracy on par with DEM [57], SPBM [70] and experimental data [71, 72, 73]. Such models can be readily interfaced with CFD simulations [74] without significant computational cost, making them ideal for three-dimensional and even turbulent flame simulations.

The MOM tracks moments of the PSD and estimates average particle properties such as mass [75], surface area [76], the number of constituent primary particles per agglomerate,  $n_p$  [67], or even particle composition [77] using the ratio of the moments. The MOM with four equations was used to describe synthesis of optical fibers by simultaneous reaction, diffusion, coagulation and thermophoresis of SiO<sub>2</sub> in laminar flow reactors assuming a lognormal PSD [78]. The MOM with interpolative closure (MOMIC) was developed to predict simultaneous nucleation, surface growth and coagulation of soot agglomerates and estimate its PSD with six equations [67]. To calculate source terms of the transported moments, additional moments that are not tracked are needed preventing the closure of the system of differential equations with the MOM [75, 79]. Thus, often the PSD shape is assumed a priori [75] or extra equations are solved to estimate it [68].

The MPBMs do not have the closure problem and calculate average particle properties by tracking their total concentration, mass [68] and area [80, 81]. Kruis et al. [68] used a 2-equation MPBM (known as the semi-empirical model) to track soot concentration and mass in (non-premixed) flames assuming spherical particles. Good agreement was achieved for measured soot mass. However, the specific surface area [81] and coagulation frequency of spheres are significantly smaller compared to that of agglomerates with the same mass underestimating their oxidation rate [70] and overestimating their concentration [40]. Kruis et al. [68] proposed a 3-equation MPBM to account for the fractal-like structure of nanoparticle agglomerates during coagulation and sintering. Agglomerate volume and area were used to obtain their equivalent primary particle diameter,  $d_p$ , and  $n_p$ . Then, agglomerate collision diameter, i.e.  $d_g$ , was calculated by  $D_f$ ,  $d_p$  and  $n_p$  to account for their fractal-like structure that affects their collision frequency. Tsantilis and Pratsinis [80] extended the MPBM to predict hard-(chemically-bonded) and soft- (physically-bonded) agglomerates during synthesis of  $\text{SiO}_2$  and  $\text{TiO}_2$  [82] nanoparticles with simultaneous reaction, surface growth, coagulation and sintering. Such a MPBM applies best at high concentrations when inception and surface growth are short [69] resulting in the dominance of coagulation where particles rapidly reach their SPSP and asymptotic fractal-like structure. This is often the case for soot emitted from a variety of combustion devices or CB reactors where inception and surface growth are limited to only a few milliseconds when temperature is very high (i.e.  $T \geq 1500\text{K}$ ) [44].

Here, we develop a computational package, called *omnisoot*, that integrates functionalities of Cantera [83] in a set of zero-dimensional reactors combined with different soot inception and surface growth models and particle dynamics models. This allows *omnisoot* to track the formation and evolution of soot coupled with gas chemistry to predict its yield, morphology, composition and size distribution. Therefore, the package can be used for fundamental understanding of soot formation including pathway analysis, reaction mechanism assessment, and the estimation of inception flux, and more importantly for process design and optimization of CB production in typical industrial reactors under different fuel compositions, temperatures, pressures and residence times. The theoretical background and governing equations for different sub-models of *omnisoot* are explained in detail. Then, the code is validated by comparing its results with benchmark DEM simulations and by ensuring elemental mass and energy balance for all models. Finally, three use cases of *omnisoot* are presented to highlight its capability in predicting gas chemistry, and soot yield, structure, and size distribution in shock-tubes, flow reactors and well-stirred reactors.

## 2 Theoretical Foundation & Governing Equations

The mathematical basis for *omnisoot* is explained in the top-to-bottom hierarchical order. The highest level is the reactors that include the transport equations of gas mixture and "soot variables". Soot formation source terms are handled by the particle dynamics model that mainly addresses particle size distribution (PSD), morphology and coagulation rate. The "*PAH growth model*" computes the contribution of inception and adsorption to source terms based on PAHs designated as precursors. Similarly, the "*surface reactions*" model obtains the surface growth and oxidation rate by HACA mechanism and passes them to the particle dynamics model.

### 2.1 Assumptions and conventions

Here, the main conventions and assumptions used in the derivation of the mathematical model are listed below.

1. The ideal gas law is used to calculate physical, transport, and chemical properties of gas mixture.
2.  $\dot{s}_k$  denotes the rate production/consumption of  $k_{th}$  gaseous species due to soot inception, surface growth and oxidation. It is positive when the species is released to gas mixture.
3. Each soot agglomerate consists of spherical monodisperse primary particles in point contact.

4. The word “*particle*” refers to soot both in spherical and agglomerate shape.
5. The density of soot is assumed constant at the value of 1800 kg/m<sup>3</sup>. Soot density changes with its maturity level, which is often linked to the elemental C/H ratio of soot particles [84]. The considered value represents an average between density of mature soot with high C/H ratio ( $\rho = 2000\text{kg/m}^3$ ) and that of nascent soot with small C/H ratios ( $\rho = 1600\text{kg/m}^3$ ) [85, 84].
6. The incipient soot particles are 2 nm in diameter, so no particles could exist with a primary particle diameter smaller than 2 nm. The number of carbon atoms in the incipient soot particle is calculated from the mass of a sphere with the diameter of 2 nm assuming pure carbon content.

$$\begin{aligned} d_{p,min} &= 2 \text{ nm} \\ n_{c,min} &= \frac{\pi}{6} \rho_{soot} d_{p,min}^3 \frac{1}{MW_c} \approx 378. \end{aligned} \quad (1)$$

7. The calculation of PAH adsorption and soot oxidation requires “*soot concentration*” which is defined as the number of soot agglomerates per unit volume of gas. The number density of agglomerates,  $N_{agg}$ , are tracked per unit mass of gas mixture i.e. *mol/kg<sub>gas</sub>*. So, soot concentration can be calculated by multiplying agglomerate number density by gas density as:

$$[\text{soot}] = \rho \cdot N_{agg}. \quad (2)$$

8. The specific heat, internal energy and enthalpy of soot are approximated by those of pure graphite, and employed to close the energy balance in the system [86].
9. Soot particles and gas are in thermal equilibrium during soot formation processes.
10. There is no temperature gradient within each agglomerate.
11. *Soot variable* refers to the features/properties of soot particles tracked by the particle dynamics model and used in the soot transport equations.
12. *PAH growth* is a unit of the soot model with a set of pathways that determine the rate of inception and adsorption from PAHs in the gas mixture.
13. *Surface reactions* is a unit of the soot model that describes the addition of acetylene to soot surface, and removal of carbon via oxidation by OH and O<sub>2</sub> in the HACA scheme. The model does not consider soot oxidation with CO<sub>2</sub>, H<sub>2</sub>O and NO<sub>x</sub>.
14. The single superscript,  $i$  denotes the section number of a soot variable or a derived property. For example,  $d_p^i$  is the primary particle diameter of section  $i$ . The double superscript,  $ij$  represents a property related to two sections. For example,  $\beta^{ij}$  is the collision frequency of the sections  $i$  and  $j$ . In the case of the monodisperse model, the section number can be ignored because it is equivalent to the sectional model with one section.
15. The computation of morphological parameters ( $d_p$ ,  $d_m$ ,  $d_g$ , and  $n_p$ ) and diffusion coefficient are done similarly by both particle dynamics models, so they are explained separately in standalone sections.
16. *precursors* refers to the PAHs larger than naphthalene used for inception and surface growth (PAH adsorption). The list of precursors with their chemical formula and molecular weight is provided in Table 1. It should be noted that the precursors can be dynamically changed by omnisooot’s user interface.

Table 1: The names, symbols, chemical formula and molecular weight of the soot precursors used by omnisoot

Species name	Symbol	Chemical formula	W [kg/mol]
Naphthalene	A2	C <sub>10</sub> H <sub>8</sub>	0.128
Phenanthrene	A3	C <sub>14</sub> H <sub>10</sub>	0.178
Pyrene	A4	C <sub>16</sub> H <sub>10</sub>	0.202
Acenaphthylene	A2R5	C <sub>12</sub> H <sub>8</sub>	0.152
Acephenanthrylene	A3R5	C <sub>16</sub> H <sub>10</sub>	0.202
Cyclopentapyrene	A4R5	C <sub>18</sub> H <sub>10</sub>	0.226

## 2.2 Constant Volume Reactor

This reactor assumes that the volume of system does not change during the process. In the absence of soot, this leads to gas with constant density. However, soot formation converts part of gaseous species to solid particles thereby affecting its volume and density. Note that, continuity, species and energy transport equations only track gas mixture properties. Figure 1 illustrates the control volume over the gas mixture targeted by mass and energy balance equations. Any mass converted to solid soot particles leaves the control volume. Mass and energy passes through the control surface around solid particles by soot formation processes. Reactor volume is the sum of volume of gas mixture and solid particles.

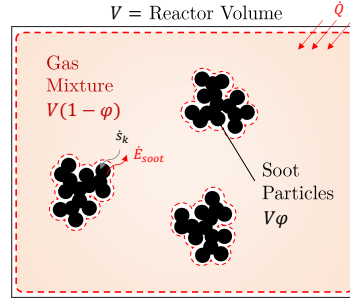


Figure 1: The schematics of control volume considered for the constant volume reactor that encompasses the gas mixture and excludes the soot particles. Mass and energy are transferred between gas and soot particles.

The continuity equation for this reactor can be written as:

$$\frac{d}{dt}(\rho(1-\varphi)) = (1-\varphi) \sum_i \dot{s}_i W_i. \quad (3)$$

Similarly, the species equation for species  $k$  is expressed as:

$$\frac{dY_k}{dt} = \frac{1}{\rho} (\dot{\omega}_k + \dot{s}_k) W_k - \frac{1}{\rho} Y_k \sum_i \dot{s}_i W_i. \quad (4)$$

The transport equation for a generic soot variable,  $\psi$  can be written as:

$$\frac{d\psi}{dt} = S_\psi - \frac{\psi}{\rho} \sum_i \dot{s}_i W_i. \quad (5)$$



The energy balance for the gas mixture can be simplified to the rate change of temperature. An external heat source of  $\dot{Q}$  is considered to account for possible heat loss/gain of the reactor.

$$\frac{dT}{dt} = \frac{1}{\rho(1-\varphi)c_v + \rho_{soot}\varphi c_{v,soot}} \left[ -(1-\varphi) \sum_k e_k (\dot{\omega}_k + \dot{s}_k) W_k + u_{soot}(1-\varphi) \sum_k \dot{s}_k W_k + \frac{\dot{Q}}{V} \right]. \quad (6)$$

### 2.3 Constant Pressure Reactor

This reactor is a closed system similar to CVR, but the pressure stays constant throughout the process and the boundaries of the system can move changing its volume. Fig.2 shows an illustration of constant pressure reactor (CPR). The heat transfer can occur through reactor walls and soot particles, which changes the internal energy of gas mixture.

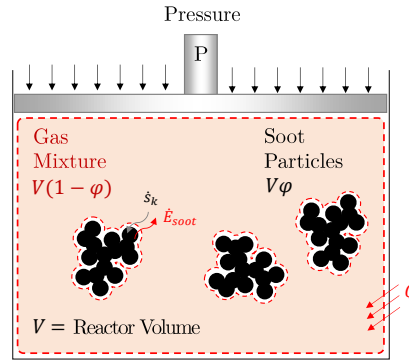


Figure 2: The schematics of control volume in the pressure reactor around the gas mixture excluding the soot particles. Mass and energy pass through the boundaries of gas and soot.

The rate change of mass, species, and soot variables for the constant pressure reactor (CPR) are the same as CVR given in Eqs. 3, 4, and 5, respectively. The energy equation is written as:

$$\frac{dT}{dt} = \frac{1}{\rho(1-\varphi)c_p + \rho_{soot}\varphi c_{p,soot}} \left[ -(1-\varphi) \sum_k h_k (\dot{\omega}_k + \dot{s}_k) W_k + h_{soot}(1-\varphi) \sum_k \dot{s}_k W_k + \frac{\dot{Q}}{V} \right]. \quad (7)$$

### 2.4 Perfectly Stirred Reactor

In this reactor, gas enters with a mass flow rate  $\dot{m}_{in}$ , composition of  $Y^*$  and temperature of  $T^*$ , instantaneously mixes and homogeneously reacts with the mixture resident inside the reactor. The reacting gas reaches a spatially uniform temperature and composition described by  $T$ , and  $Y$ . It is assumed that temperature, composition and soot properties of the outflow are the same as reactor. Figure 3 illustrates the schematics of PSR.  $\dot{m}_{in}$  and  $\dot{m}_{out}$  refer to inflow and outflow gas mass flow rates, respectively. Under no-soot conditions, the inlet and outlet mass flow rates are equal, but the gas mixture loses mass by soot formation, so  $\dot{m}_{out}$  is slightly less than  $\dot{m}_{in}$ . The pressure of reactor is assumed to stay constant during the process [87]. The nominal residence time of gas mixture in the reactor is defined as:

$$\tau = \frac{\rho V}{\dot{m}_{in}}. \quad (8)$$



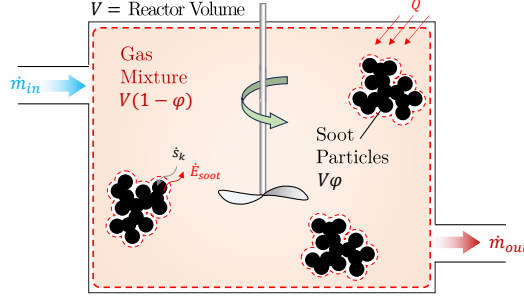


Figure 3: The schematics of control volume considered for the perfectly stirred reactor that encompasses the gas mixture and excludes the soot particles. Mass and energy are transferred between gas and soot particles. The inlet flow brings species and enthalpy into the control volume and the outflow discharges them. The gas mass flow at the outlet is less inlet due to partial conversion of gaseous species to soot.

The conservation of mass can be written for PSR by considering the mass flux of in- and outflow, and the removal of mass due to soot generation as:

$$\frac{dm}{dt} = \dot{m}_{in} - \dot{m}_{out} + (1 - \varphi) \sum_i \dot{s}_i W_i. \quad (9)$$

The density is not determined by solving the continuity equation, but rather from ideal gas law and assuming a constant pressure and the composition from solving the species transport equations as:

$$\frac{dY_k}{dt} = \frac{1}{\tau} (Y_k^* - Y_k) + \frac{1}{\rho} \left[ (\dot{\omega}_k + \dot{s}_k) W_k - Y_k \sum_i \dot{s}_i W_i \right]. \quad (10)$$

The soot transport equations can also be expressed as:

$$\frac{d\psi}{dt} = \frac{\dot{m}_{in}}{\rho V (1 - \varphi)} (\psi^* - \psi) + S_\psi - \frac{1}{\rho} \psi \sum_i \dot{s}_i W_i. \quad (11)$$

The energy equation for this reactor is written as:

$$\begin{aligned} \frac{dT}{dt} = \frac{1}{\rho (1 - \varphi) c_p + \rho_{soot} c_{p,soot} \varphi} & \left[ \frac{\dot{m}_{in}}{V} (h^* - h) - \frac{\dot{m}_{in}}{V} \sum_k (Y_k^* - Y_k) h_k \right. \\ & \left. - (1 - \varphi) \sum_k (\dot{\omega}_k + \dot{s}_k) W_k h_k + (1 - \varphi) \sum_i \dot{s}_i W_i h_{soot} + \frac{\dot{Q}}{V} \right]. \end{aligned} \quad (12)$$

## 2.5 Plug Flow Reactor

The plug flow reactor (PFR) is an ideal representation of a channel or duct with a constant cross-sectional area where a steady-state one-dimensional flow changes temperature, composition, and soot properties along the channel. There is no spatial gradient over the cross-section due to strong mixing. Diffusion along the channel is negligible. The pressure is assumed constant along the reactor.

The continuity equation for PFR is written as:

$$\frac{d}{dz} (\rho u (1 - \varphi)) = (1 - \varphi) \sum_i \dot{s}_i W_i. \quad (13)$$

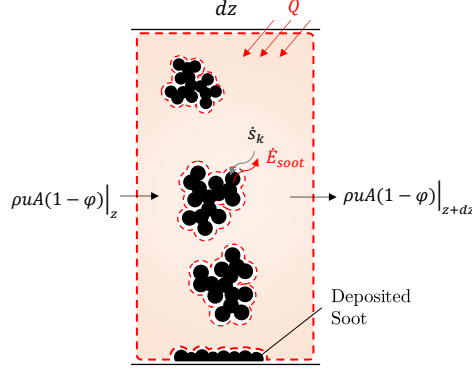


Figure 4: The schematics of control volume for a differential element along PFR that includes the gas mixture and excludes the soot particles considering wall heat transfer. The model considers mass and energy are transfer between gas and soot as well as wall deposition along the reactor.

The momentum equation can also be established as:

$$u(1-\varphi) \sum_i \dot{s}_i W_i + \rho u(1-\varphi) \frac{du}{dz} = -\frac{d}{dz}(p(1-\varphi)) - \frac{\tau_w}{R_H}. \quad (14)$$

where  $\tau_w$  is the wall shear the can be determined from fraction factor,  $f$  as:

$$\tau_w = \frac{1}{2} \rho u^2 f. \quad (15)$$

The friction factor,  $f$  can be calculated with a good accuracy for the entire range of Reynolds number,  $Re$ , from laminar to turbulent flow using the explicit formula given by Haaland [88]:

$$\frac{1}{f^{1/2}} = -1.8 \log \left( \frac{6.9}{Re} + \left[ \frac{\epsilon/D_H}{3.7} \right]^{1.11} \right), \quad (16)$$

where  $\epsilon$  is the roughness of reactor wall.  $R_H$  and  $D_H$  are hydraulic radius and diameter, respectively that can be determined from cross-section geometry of reactor as:

$$D_H = 4R_H = \frac{4A_c}{P_c}, \quad (17)$$

$A_c$  and  $P_c$  are cross-sectional area and wetted perimeter of the reactor. The species equation can be expressed as:

$$\frac{dY_k}{dz} = \frac{1}{\rho u} \left[ (\dot{\omega}_k + \dot{s}_k) W_k - Y_k \sum_i \dot{s}_i W_i \right]. \quad (18)$$

The soot transport equations can also be written as:

$$\frac{d\psi}{dz} = \frac{S_\psi}{u} - \frac{\psi}{\rho u} \sum_i \dot{s}_i W_i - \frac{4}{D_H} \frac{k_{dep}^i \psi}{u}. \quad (19)$$

where  $k_{dep}^i$  is the deposition velocity of soot particles of section  $i$  calculated as:

$$k_{dep} = \frac{Sh \cdot D^i}{D_H}. \quad (20)$$

where  $Sh$  is the Sherwood number, which is 3.66 for a laminar flow and calculated using the Berger and Hau correlation [89] for the turbulent flow in terms of  $Re$  and  $Sc$ , Schmidt number as:

$$Sh = 0.0165Re^{0.86}Sc^{1/3}. \quad (21)$$

The energy equation can be expressed as:

$$\frac{dT}{dz} = \frac{1}{\rho u(1-\varphi)c_p + \rho_{soot}u\varphi c_{p,soot}} \left[ -(1-\varphi) \sum_k h_k (\dot{\omega}_k + \dot{s}_k) W_k + h_{soot}(1-\varphi) \sum_k \dot{s}_k W_k + q'' \frac{P_c}{A_c} \right]. \quad (22)$$

where  $q''$  is the wall heat flux provided as a function of reactor length or flow residence time that represents external heating or heat loss in the reactor.

### 3 Particle Dynamics

Population balance models rely on the Eulerian description of particles where bulk properties of particle population such as number density, mass or surface area are treated as continuous quantities and tracked by solving scalar transport equations. These methods are computationally cheaper compared with mesoscale models such as DEM, and can be easily interfaced with chemical kinetics in CFD solvers to simulate soot formation in turbulent configurations. Here, we use two particle dynamics models: a monodisperse population balance model (MPBM) based on four variables leading to 4 transport equations in total, and a fixed sectional population balance model (SPBM) tracking three variables per section. The total number of transport equations in the sectional model is determined by the number of sections and number of equations solved per section. The first two/three variables in the MPBM/SPBM enables description of number, mass, and evolving fractal-like morphology of soot agglomerates that are necessary to accurately predict collision frequency of agglomerates [90] as well as oxidation and surface growth rates [70]. The last variable tracks the number of hydrogen atoms in agglomerates that allows the model to capture the soot composition, thereby its maturity [32], and surface reactivity [77]. The tracked variables are used to address particle dynamics that includes (i) reconstructing particles morphology by determining characteristic diameters from tracked soot variables, (ii) calculating collision frequency and coagulation source term, (iii) combining the contribution of inception, PAH adsorption, surface growth and oxidation into source terms. First, common features of both particle dynamics models are reviewed. As mentioned before, any parameter with superscript  $i$  denotes the section number, which can be ignored/dropped for the MPBM that only has one section. For example,  $d_m^i$  can be replaced with  $d_m$ .

#### 3.1 Soot Morphology

The evolving fractal-like structure of agglomerates is quantified by their mobility diameter normalized by primary particle,  $d_m/d_p$ , and gyration,  $d_m/d_g$ , diameters that can be described with power-laws derived from mesoscale simulations. Incipient soot is initially a sphere formed of PAHs with constant density that grows in size by surface reactions and forms agglomerates by coagulation. The collision frequency of particles depends on their evolving fractal-like structure [90]. Some simplifying assumptions are made to reconstruct the particle morphology from tracked variables. The primary particles of each agglomerate are similar enough that can be described by mean size and composition. They also stay in point contact during surface growth and agglomeration i.e. the necking is ignored. A universal fractal dimension,  $D_f = 1.9$  is used for agglomerates larger than sphere [91]. Mobility and gyration diameters are the diameter of a sphere with the same translational and rotational properties of the agglomerate, respectively. The employed power-laws have been shown to describe the morphology of soot from premixed [71], diffusion [92] flames, and diesel engines [93]. Figure 5 illustrates the schematics of a soot agglomerates with 12 primary particles and depicted  $d_p$ ,  $d_m$ , and  $d_g$ .

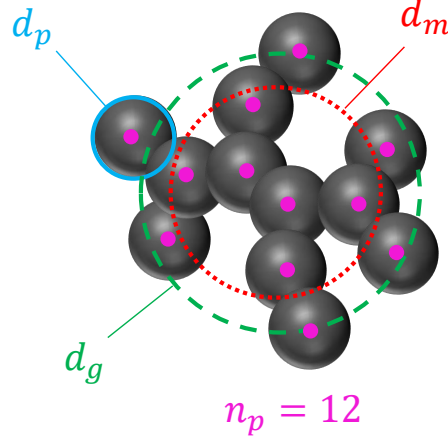


Figure 5: The schematics of a soot agglomerates with 12 primary particles ( $n_p = 12$ ). Primary particle ( $d_p$ ), mobility ( $d_m$ ), and gyration ( $d_g$ ) are shown.

$n_p^i$  is the number of primary particles per agglomerate for  $i^{\text{th}}$  section that can be obtained by dividing the number density of primary particles by the the number density of agglomerates of that section as:

$$n_p^i = \frac{N_{pri}^i}{N_{agg}^i}. \quad (23)$$

Primary particle diameter,  $d_p^i$ , can be obtained from total carbon content and number density of primary particles using

$$d_p^i = \left( \frac{6}{\pi} \frac{C_{tot}^i \cdot W_{carbon}}{\rho_{soot}} \frac{1}{N_{pri}^i \cdot Av} \right)^{1/3}. \quad (24)$$

The DEM-derived power-laws [55] relate  $d_m^i$  and  $d_g^i$  to  $d_p^i$  and  $n_p^i$  as

$$d_m^i = d_p^i \cdot n_p^{i 0.45}, \quad (25)$$

$$d_g^i = \begin{cases} d_m^i / (n_p^{i -0.2} + 0.4), & \text{if } n_p^i > 1.5 \\ d_m^i / 1.29. & \text{if } n_p^i \leq 1.5 \end{cases} \quad (26)$$

The collision diameter,  $d_c^i$  is the maximum of  $d_m^i$ ,  $d_g^i$ :

$$d_c^i = \max(d_m^i, d_g^i) \quad (27)$$

$d_m^i$ ,  $d_g^i$ ,  $d_c^i$  are used to calculate the source terms due to the surface growth, oxidation, PAH adsorption and coagulation. The volume equivalent diameter,  $d_v^i$ , is the diameter of the sphere with the same mass as agglomerate, and it is obtained as:

$$d_v^i = d_p^i \cdot n_p^{i 1/3} \quad (28)$$

The primary particle surface area is calculated from  $d_p^i$  assuming spherical primary particles.

$$A_p^i = \pi d_p^{i 2}, \quad (29)$$

$A_{tot}^i$  (for each section) is defined as the total surface area of soot particles per unit mass of gas mixture obtained as

$$A_{tot}^i = N_{pri}^i \cdot Av \cdot A_p^i. \quad (30)$$

### 3.2 Diffusion of soot particles

The diffusion coefficient of soot particle,  $D^i$ , is calculated as

$$D^i = \frac{k_B T}{f^i}, \quad (31)$$

where  $f^i$  is the friction factor of particles in gas,

$$f^i = \frac{3\pi\mu d_m^i}{C^i(d_m^i)}, \quad (32)$$

where  $C^i$  is the Cunningham function that corrects the friction factor given a diameter in the continuum regime for transition and free molecular regimes as:

$$C^i(d) = 1 + \frac{2\lambda}{d} \left( 1.21 + 0.4 \cdot \exp\left(\frac{-0.78d}{\lambda}\right) \right), \quad (33)$$

where  $\lambda$  is the mean free path of gas given as:

$$\lambda = \frac{\mu}{\rho} \sqrt{\frac{\pi W_{gas}}{2k_B A v T}}. \quad (34)$$

Note that,  $\lambda$  is a property of the gas mixture that does not depend on particle morphology and size section. The mean velocity,  $c^i$  and mean stop distance of particles,  $\lambda_a^i$  can be calculated as:

$$c^i = \sqrt{\frac{8k_B T}{\pi m_{agg}^i}}. \quad (35)$$

$$\lambda_a = \frac{8D^i}{\pi c^i}. \quad (36)$$

The mean distance of particles are also calculated as:

$$\delta_a^i = \frac{1}{d_c^i \lambda_a^i} \left[ (d_c^i + \lambda_a^i)^3 - (d_c^{i2} + \lambda_a^{i2})^{3/2} \right] - d_{c,j}. \quad (37)$$

### 3.3 Coagulation efficiency of soot particles

The coagulation efficiency of soot particles is commonly assumed as unity meaning that every collision between two soot particles successfully results in formation of a new agglomerate. However, numerical models [94] and experimental evidence [95] showed that the coagulation efficiency can significantly change with particle size and temperature drastically decreasing for particles smaller than 10 nm in the free molecular regime ( $Kn \gg 10$ ) due to their high kinetic energy that excess the attractive forces [96]. The coagulation efficiency of two colliding particles can be described as Narsimhan and Ruckenstein [94]:

$$\zeta^{ij} = 1 - \left( 1 + \frac{\Phi_0^{ij}}{k_B T} \right) \exp \left( -\frac{\Phi_0^{ij}}{k_B T} \right), \quad (38)$$

where  $\Phi_0$  is the potential well depth i.e. the minimum interaction energy between two colliding particles. Hou et al. [97] calculated  $\Phi_0$  for soot particles 1-15 nm by considering the attraction and repulsion between constituent carbon and hydrogen atoms, and proposed a equation based on the reduced diameter,  $d_r^{jk}$  of colliding particles as:

$$\Phi_0^{ij} = -6.6891 \times 10^{-23} (d_r^{jk})^3 + 1.244 \times 10^{-21} (d_r^{jk})^2 + 1.1394 \times 10^{-20} d_r^{jk} - 5.5373 \times 10^{-21} \quad (39)$$

$$d_r^{jk} = \frac{d_c^i + d_c^j}{d_c^i + d_c^j} \quad (40)$$

Eq. (39) is valid for  $d_r^{jk}$  between 1 and 7 nm, and  $\zeta^{ij}$  is assumed as 1 for particles with reduced diameter larger than 7 nm.

### 3.4 Soot Composition

The composition of soot is characterized by their elemental carbon to hydrogen ratio (C/H) is a measure of soot maturity and increases from  $C/H < 2$  for incipient soot [98] to  $2 < C/H < 10$  for nascent soot [99] and  $C/H > 20$  for mature soot [100]. The soot agglomerates are assumed to have pure carbon graphitic core [32] with all hydrogen atoms on the surface [77]. C/H ratio can be obtained from total carbon and hydrogen content as:

$$\left(\frac{C}{H}\right)^i = \frac{C_{tot}^i}{H_{tot}^i}. \quad (41)$$

The carbon content of each agglomerate is a predefined parameter in the SPBM (depending on the section the agglomerate is placed), but it can be calculated from dividing  $C_{tot}$  by  $N_{agg}$  for the MPBM. The hydrogen content of each agglomerate is calculated for both particle dynamics models as:

$$H_{agg}^i = \frac{H_{tot}^i}{N_{agg}^i}. \quad (42)$$

### 3.5 Monodisperse Population Balance Model

The MPBM used in this research tracks the number density of primary particles ( $N_{pri}$ ) and agglomerates ( $N_{agg}$ ), total carbon ( $C_{tot}$ ) and hydrogen ( $H_{tot}$ ) content of soot particles per unit mass of gas mixture. The morphological parameters such as primary particle, mobility and gyration diameters obtained from these soot variables are the average values for the population.

#### 3.5.1 Coagulation

Coagulation is the process during which solid and hard soot particles collide and attach at point of contact leading to larger agglomerates. This process conserves the soot mass and composition and number density of primary particles, so coagulation only affects  $N_{agg}$ .  $I_{coag}^N$  accounts for the decay rate of  $N_{agg}$  by the binary collision of soot particles by

$$I_{coag} = -\frac{1}{2}\zeta\beta N_{agg}^2, \quad (43)$$

where  $\beta$  is the collision frequency of agglomerates for the free molecular ( $Kn > 10$ ) to continuum regime ( $Kn < 0.1$ ), and  $\zeta$  is the coagulation efficiency explained in Sec.3.3. The value of  $\beta$  in the transition regime ( $0.1 < Kn < 10$ ) can be calculated from the harmonic mean of the continuum ( $\beta_{cont}$ ) and free molecular ( $\beta_{fm}$ ) regime values. Additionally, an enhancement factor of 1.82 is applied to take into account the effect of polydispersity [56] as:

$$\beta = 1.82 \frac{\beta_{fm}\beta_{cont}}{\beta_{fm} + \beta_{cont}}, \quad (44)$$

$$\beta_{fm} = 4\sqrt{\frac{\pi k_b T}{m_{agg}}} d_c^2, \quad (45)$$

$$\beta_{cont} = 8\pi d_c D. \quad (46)$$

Alternatively,  $\beta$  can be obtained using Fuchs interpolation [101] as:

$$\beta = \beta_{cont} \left( \frac{d_c}{d_c + 2\sqrt{2}\delta} + \frac{8D}{\sqrt{2}c_r d_c} \right)^{-1}. \quad (47)$$

### 3.5.2 Source terms

The source terms of tracked variables combines the effect of the inception, PAH adsorption, surface growth and oxidation and coagulation.

$$S_{N_{agg}} = \frac{I_{N,inc}}{n_{c,min}} + I_{coag}. \quad (48)$$

$$S_{N_{pri}} = \frac{I_{N,inc}}{n_{c,min}}. \quad (49)$$

$$S_{C_{tot}} = I_{C_{tot},inc} + I_{C_{tot},gr} + I_{C_{tot},ads} + I_{C_{tot},ox}. \quad (50)$$

$$S_{H_{tot}} = I_{H_{tot},inc} + I_{H_{tot},gr} + I_{H_{tot},ads} + I_{H_{tot},ox}. \quad (51)$$

The partial source terms in Equations 48-51 denoted by I are determined by PAH growth and surface reaction model explained in Sections 5 and 4, respectively.

## 3.6 Sectional Population Balance Model

A SPBM with the fixed pivot is used to describe particle dynamics [102]. The mass range of particles are divided into discrete sections each of which includes agglomerates of the same mass. Inception introduces new particles to the first section with the mass corresponding to the incipient particle. The particles of first section can migrate to upper sections by gaining mass via surface growth and coagulation, and return to lower sections when they lose mass through oxidation. The mass of sections is determined by a geometric progression with a scale factor equal to the mass of incipient soot particle, and a common ratio of SF, known as sectional spacing factor. The mass of each section is approximated by the carbon content of agglomerates in moles as:

$$C_{agg}^i = \frac{n_{c,min}}{Av} \cdot SF^{(i-1)}. \quad (52)$$

where (i-1) represents the exponent of SF. The mass of hydrogen is ignored in the placement of agglomerates in the sections. The total number density of agglomerates,  $N_{agg}^i$  [mol/kg], and primary particles,  $N_{pri}^i$  [mol/kg] are tracked for each section. Morphological parameters are determined for each section according to the equations in Section 3.1.

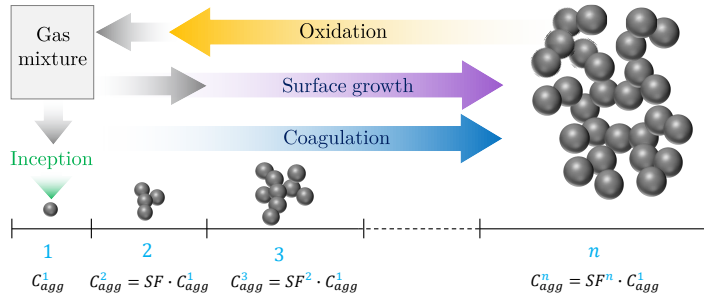


Figure 6: The illustration of sections of SPBM. The mass of sections grows progressively by the scale factor of SF. Inception introduces new particles to the first section that propagate to the upper section via coagulation and surface growth and return to lower sections by oxidation



### 3.6.1 Coagulation

In SPBM approach, collisions between particles from every two sections are considered. The new particles formed by coagulation are placed in a upper section with the mass equal to sum of mass of particles involved in the collision. When the mass of yielded particle lies between two consecutive sections, the particles are divided among these sections proportional to their mass. One possible scenario is that the mass of the newly formed particle is greater than the last section, thus leaving tracked mass range. Losing mass is a potential problem with the fixed pivot sectional model, which can be avoided by selecting proper number of sections and spacing factor to ensure the last sections stay empty during the simulation.

The collision frequency between sections  $j$  and  $k$  can be obtained from the harmonic mean of the values in the continuum and free molecular regimes as:

$$\beta^{jk} = \frac{\beta_{fm}^{jk} \beta_{cont}^{jk}}{\beta_{fm}^{jk} + \beta_{cont}^{jk}}, \quad (53)$$

$$\beta_{fm}^{jk} = \sqrt{\frac{\pi k_b T}{2} \left( \frac{1}{m_{agg}^j} + \frac{1}{m_{agg}^k} \right)} (d_c^j + d_c^k)^2, \quad (54)$$

$$\beta_{cont}^{ij} = \frac{2k_B T}{3\mu} \left( \frac{C^j}{d_m^j} + \frac{C^k}{d_m^k} \right) (d_c^j + d_c^k)^2. \quad (55)$$

The collision frequency can also be determined from the Fuchs interpolation similar to the MPBM as:

$$\beta^{jk} = \beta_{cont}^{ij} \left[ \frac{d_c^j + d_c^k}{d_c^j + d_c^k + 2 + \delta_r^{jk}} + \frac{8(D^j + D^k)}{\bar{c}_r^{jk} (d_c^j + d_c^k)} \right]^{-1}, \quad (56)$$

where  $\delta_r^{jk}$  and  $\bar{c}_r^{jk}$  are the mean square root of mean distance and velocity of particles, respectively.

$$\delta_r^{jk} = \sqrt{\delta_a^{j2} + \delta_a^{k2}}, \quad (57)$$

$$\bar{c}_r^{jk} = \sqrt{c^{j2} + c^{k2}}. \quad (58)$$

Coagulation redistributes the total number of agglomerates and primary particles as well as hydrogen atoms among the sections. The partial coagulation source terms for  $N_{agg}^i$ ,  $N_{pri}^i$  and  $H_{tot}^i$  can be calculated as:

$$I_{N_{agg}}^i = \sum_{k=1}^{n_{sec}} \sum_{j=k}^{n_{sec}} \left( 1 - \frac{\delta_{jk}}{2} \right) \eta_{ijk} \zeta^{jk} \beta^{jk} N_{agg}^j N_{agg}^k - N_{agg}^i \sum_{k=1}^{n_{sec}} \zeta^{im} \beta^{im} N_{agg}^m. \quad (59)$$

$$I_{N_{pri}}^i = \sum_{k=1}^{n_{sec}} \sum_{j=k}^{n_{sec}} \left( 1 - \frac{\delta_{jk}}{2} \right) \eta_{p,ijk} \eta_{ijk} \zeta^{jk} \beta^{jk} N_{agg}^j N_{agg}^k - N_{pri}^i \sum_{k=1}^{n_{sec}} \zeta^{im} \beta^{im} N_{agg}^m. \quad (60)$$

$$I_{H_{tot}}^i = \sum_{k=1}^{n_{sec}} \sum_{j=k}^{n_{sec}} \left( 1 - \frac{\delta_{jk}}{2} \right) \eta_{h,ijk} \eta_{ijk} \zeta^{jk} \beta^{jk} N_{agg}^j N_{agg}^k - H_{tot}^i \sum_{k=1}^{n_{sec}} \zeta^{im} \beta^{im} N_{agg}^m. \quad (61)$$

where  $\delta_{jk}$  is the Kronecker delta defined as:

$$\delta_{jk} = \begin{cases} 1, & \text{if } j = k \\ 0, & \text{if } j \neq k \end{cases} \quad (62)$$

In Equation (59),  $\eta_{ijk}$  assigns newly formed agglomerates to the two consecutive section in order to conserves mass during coagulation [60].

$$\eta_{ijk} = \begin{cases} \frac{C_{agg}^{i+1} - C_{agg}^{jk}}{C_{agg}^{i+1} + C_{agg}^i}, & \text{if } C_{agg}^i \leq C_{agg}^{jk} < C_{agg}^{i+1} \\ \frac{C_{agg}^i - C_{agg}^{jk}}{C_{agg}^i + C_{agg}^{i-1}}, & \text{if } C_{agg}^{i-1} \leq C_{agg}^{jk} < C_{agg}^i \\ 0 & \text{else} \end{cases} \quad (63)$$

where  $C_{agg}^{jk} = C_{agg}^j + C_{agg}^k$ . Similarly,  $\eta_{p,ijk}$  in Equation (60) and  $\eta_{h,ijk}$  in Equation (61) adjust the number primary particles and hydrogen atoms added to consecutive sections based on their mass, respectively.

$$\eta_{p,ijk} = \frac{C_{agg}^i}{C_{agg}^{jk}} (n_p^j + n_p^k), \quad (64)$$

$$\eta_{h,ijk} = \frac{C_{agg}^i}{C_{agg}^{jk}} (H_{agg}^j + H_{agg}^k), \quad (65)$$

### 3.6.2 Source terms

The source terms are split into four parts showing the contribution of different soot formation and evolution factors. The effect of surface growth and PAH adsorption are combined (denoted by the subscript gr,ads) because they are similar mass-gaining mechanisms.

$$S_{N_{agg}} = (S_{N_{agg}})_{inc} + (S_{N_{agg}})_{gr,ads} + (S_{N_{agg}})_{ox} + (S_{N_{agg}})_{coag}, \quad (66)$$

$$S_{N_{pri}} = (S_{N_{pri}})_{inc} + (S_{N_{pri}})_{gr,ads} + (S_{N_{pri}})_{ox} + (S_{N_{pri}})_{coag}, \quad (67)$$

$$S_{H_{tot}} = (S_{H_{tot}})_{inc} + (S_{H_{tot}})_{gr,ads} + (S_{H_{tot}})_{ox} + (S_{H_{tot}})_{coag}. \quad (68)$$

Inception introduces equal number of agglomerates and primary particles to the first section.

$$(S_{N_{agg}})_{inc} = \frac{1}{Av} \frac{I_{N,inc}}{C_{agg}^i}, \quad i = 1. \quad (69)$$

$$(S_{N_{pri}})_{inc} = \frac{1}{Av} \frac{I_{N,inc}}{C_{agg}^i}, \quad i = 1. \quad (70)$$

$$(S_{H_{tot}})_{inc} = I_{H,inc}, \quad i = 1. \quad (71)$$

Surface growth and PAH adsorption increase the (carbon) mass and hydrogen content of agglomerates, and transfer them to upper sections. The removal rate of agglomerates ( $N_{agg}^i$ ) from the original section due to surface growth and PAH adsorption must be equal to the addition rate of agglomerates to the target section to conserve the mass, and it is calculated by dividing the mass growth rate by the difference of the mass of the adjacent sections.

$$(S_{N_{agg}})_{gr,ads} = \frac{1}{Av} \begin{cases} -\frac{I_{C_{tot},gr}^i + I_{C_{tot},ads}^i}{C_{agg}^{i+1} - C_{agg}^i} & \text{if } i = 1 \\ \frac{I_{C_{tot},gr}^{i-1} + I_{C_{tot},ads}^{i-1}}{C_{agg}^i - C_{agg}^{i-1}} - \frac{I_{C_{tot},gr}^i + I_{C_{tot},ads}^i}{C_{agg}^{i+1} - C_{agg}^i} & \text{if } 1 < i < n_{sec} \\ \frac{I_{C_{tot},gr}^{i-1} + I_{C_{tot},ads}^{i-1}}{C_{agg}^i - C_{agg}^{i-1}} & \text{if } i = n_{sec} \end{cases} \quad (72)$$

As agglomerates move up/down through sections, they carry the number of primary particles as well as hydrogen atoms, so the transfer rate of agglomerates is multiplied by  $n_p^i$  and  $H_{agg}^i$ , respectively.

$$(S_{N_{pri}})_{gr,ads} = \frac{1}{Av} \begin{cases} -\frac{I_{C_{tot},gr}^i + I_{C_{tot},ads}^i}{C_{agg}^{i+1} - C_{agg}^i} & \text{if } i = 1 \\ \frac{I_{C_{tot},gr}^{i-1} + I_{C_{tot},ads}^{i-1}}{C_{agg}^i - C_{agg}^{i-1}} n_p^{i-1} - \frac{I_{C_{tot},gr}^i + I_{C_{tot},ads}^i}{C_{agg}^{i+1} - C_{agg}^i} n_p^i & \text{if } 1 < i < n_{sec} \\ \frac{I_{C_{tot},gr}^{i-1} + I_{C_{tot},ads}^{i-1}}{C_{agg}^i - C_{agg}^{i-1}} n_p^{i-1} & \text{if } i = n_{sec} \end{cases} \quad (73)$$

$$(S_{H_{tot}})_{gr,ads} = \frac{1}{Av} \begin{cases} -\frac{I_{C_{tot},gr}^i + I_{C_{tot},ads}^i}{C_{agg}^{i+1} - C_{agg}^i} H_{agg}^i + I_{H_{tot},gr}^i + I_{H_{tot},ads}^i & \text{if } i = 1 \\ \frac{I_{C_{tot},gr}^{i-1} + I_{C_{tot},ads}^{i-1}}{C_{agg}^i - C_{agg}^{i-1}} H_{agg}^{i-1} - \frac{I_{C_{tot},gr}^i + I_{C_{tot},ads}^i}{C_{agg}^{i+1} - C_{agg}^i} H_{agg}^i + I_{H_{tot},gr}^i + I_{H_{tot},ads}^i & \text{if } 1 < i < n_{sec} \\ \frac{I_{C_{tot},gr}^{i-1} + I_{C_{tot},ads}^{i-1}}{C_{agg}^i - C_{agg}^{i-1}} H_{agg}^{i-1} + I_{H_{tot},gr}^i + I_{H_{tot},ads}^i & \text{if } i = n_{sec} \end{cases} \quad (74)$$

Similarly, the agglomerates lose (carbon) mass by oxidation, and descend to the lower sections carrying primary particle and hydrogen.

$$(S_{N_{agg}})_{ox} = \frac{1}{Av} \begin{cases} \frac{I_{C_{tot},ox}^{i+1}}{C_{agg}^{i+1} - C_{agg}^i} - \frac{I_{C_{tot},ox}^i}{C_{agg}^i} & \text{if } i = 1 \\ \frac{I_{C_{tot},ox}^{i+1}}{C_{agg}^{i+1} - C_{agg}^i} - \frac{I_{C_{tot},ox}^i}{C_{agg}^i - C_{agg}^{i-1}} & \text{if } 1 < i < n_{sec} \\ -\frac{I_{C_{tot},ox}^i}{C_{agg}^i - C_{agg}^{i-1}} & \text{if } i = n_{sec} \end{cases} \quad (75)$$

$$(S_{N_{pri}})_{ox} = \frac{1}{Av} \begin{cases} \frac{I_{C_{tot},ox}^{i+1}}{C_{agg}^{i+1} - C_{agg}^i} n_p^{i+1} - \frac{I_{C_{tot},ox}^i}{C_{agg}^i} & \text{if } i = 1 \\ \frac{I_{C_{tot},ox}^{i+1}}{C_{agg}^{i+1} - C_{agg}^i} n_p^{i+1} - \frac{I_{C_{tot},ox}^i}{C_{agg}^i - C_{agg}^{i-1}} n_p^i & \text{if } 1 < i < n_{sec} \\ -\frac{I_{C_{tot},ox}^i}{C_{agg}^i - C_{agg}^{i-1}} n_p^i & \text{if } i = n_{sec} \end{cases} \quad (76)$$

$$(S_{H_{tot}})_{ox} = \frac{1}{Av} \begin{cases} \frac{I_{C_{tot},ox}^{i+1}}{C_{agg}^{i+1} - C_{agg}^i} H_{agg}^{i+1} - \frac{I_{C_{tot},ox}^i}{C_{agg}^i} H_{agg}^i + I_{H_{tot},ox}^i & \text{if } i = 1 \\ \frac{I_{C_{tot},ox}^{i+1}}{C_{agg}^{i+1} - C_{agg}^i} H_{agg}^{i+1} - \frac{I_{C_{tot},ox}^i}{C_{agg}^i - C_{agg}^{i-1}} H_{agg}^i + I_{H_{tot},ox}^i & \text{if } 1 < i < n_{sec} \\ -\frac{I_{C_{tot},ox}^i}{C_{agg}^i - C_{agg}^{i-1}} H_{agg}^i + I_{H_{tot},ox}^i & \text{if } i = n_{sec} \end{cases} \quad (77)$$

## 4 Surface reactions model

The heterogeneous surface reactions are described by hydrogen-abstraction-acetylene-addition (HACA) mechanism [27, 47]. The soot growth in HACA scheme is based on a sequential process similar to

PAH growth. The hydrogenated arm-chair sites ( $C_{\text{soot}} - H$ ) on the edge of aromatic rings are dehydrogenated by H abstraction forming  $C_{\text{soot}}^\circ$  that bonds with  $C_2H_2$  resulting in an additional aromatic ring with hydrogenated site. These sites can also be attacked by  $O_2$  or  $OH$ . The elementary reactions that describe this sequential process are listed in Table 2. The rate of mass growth by HACA is obtained from the reaction of  $C_2H_2$  with dehydrogenated sites as:

$$\omega_{gr}^i = \alpha^i k_{f4} [C_2H_2] [C_{\text{soot}}^\circ]. \quad (78)$$

where  $k_{f4}$  denotes the forward rate of Reaction 2 in Table 2, and  $[C_{\text{soot}}^\circ]$  is obtained by multiplying the surface density of dehydrogenated sites,  $\chi_{\text{soot}}^\circ$  with total surface area of soot (per unit of mass of gas mixture) as:

$$[C_{\text{soot}}^\circ] = \frac{\rho}{A_v} A_{\text{tot}}^i \cdot \chi_{\text{soot}}^\circ. \quad (79)$$

$\chi_{\text{soot}}^\circ$  is calculated by assuming the steady-state for  $[C_{\text{soot}}^\circ]$  in the system of reactions in Table 2:

$$\chi_{\text{soot}}^\circ = \frac{k_{f1} [H] + k_{f2} [OH]}{k_{r1} [H_2] + k_{r2} [H_2O] + k_{f3} [H] + k_{f4} [C_2H_2] + k_{f5} [O_2] + k_{f1} [H] + k_{f2} [OH]} \chi_{\text{soot}_{CH}}, \quad (80)$$

where  $\chi_{\text{soot}_{CH}}$  is the surface density of hydrogenated sites estimated based on the assumption that soot surface is covered with stacks of benzene rings [47]. Considering the stack spacing of 3.15 Å and 2 C-H bonds per benzene ring length, the surface density of hydrogenated sites,  $\chi_{\text{soot}-H}$ , is calculated to be  $0.23 \text{ site}/\text{\AA}^2 = 2.3 \times 10^{19} \text{ site}/\text{m}^2$ , which gives the maximum theoretical limit of the reaction sites.

In Equation (78),  $\alpha$  is the surface reactivity factor between 0 and 1 that represents the decline of reaction sites from the theoretical limit due to particle aging, growth and maturity [103, 104], and it has been observed to depend on temperature time history [105, 49]. The value of  $\alpha$  has been described using constant target-specific values as well as empirical equations based on particle size and flame temperature. A detailed review of these can be found in the chapter 4 of [106]. Here, the empirical equations proposed by Appel et al. [47] is used to calculate  $\alpha$ :

$$\alpha^i = \tanh \left( \frac{12.56 - 0.00563 \cdot T}{\log_{10} \left( \frac{\rho_{\text{soot}} \cdot A_v}{W_{\text{carbon}}} \frac{\pi}{6} d_p^3 \right)} - 1.38 + 0.00068 \cdot T \right). \quad (81)$$

Alternatively, Blanquart and Pitsch [76] related  $\alpha$  to the number of surface hydrogen atoms on the soot particles.

$$\alpha^i = \frac{H_{\text{tot}}^i}{C_{\text{tot}}^i}. \quad (82)$$

The contribution of HACA to growth source terms can be computed from HACA rates considering the number of carbon atoms in  $C_2H_2$  and number of arm-chair and zig-zag hydrogenated sites on soot particle [77] using

$$I_{C_{\text{tot}},gr}^i = 2\omega_{gr}^i / \rho, \quad (83)$$

$$I_{H_{\text{tot}},gr}^i = 0.25\omega_{gr}^i / \rho. \quad (84)$$

The rate change of  $C_2H_2$  concentration due to mass growth is written as:

$$\left( \frac{d[C_2H_2]}{dt} \right)_{gr} = - \sum_{i=1}^{n_{sec}} \omega_{gr}^i. \quad (85)$$

The rate of release of H radicals into the gas mixture due to surface growth is:

$$\left( \frac{d[H]}{dt} \right)_{gr} = 1.75 \sum_{i=1}^{n_{sec}} \omega_{gr}^i. \quad (86)$$

Table 2: Rate coefficients for the various surface reactions in Arrhenius form  $k = AT^n \cdot e^{-E/RT}$

No.	Reaction		A $\left[\frac{\text{m}^3}{\text{mol}\cdot\text{s}}\right]$	n	$\frac{E}{R}$ [K]
(R1)	$\text{C}_{\text{soot-H}} + \text{H} \rightleftharpoons \text{C}_{\text{soot}^\circ} + \text{H}_2$	f	$4.17 \times 10^7$	0	6542.52
		r	$3.9 \times 10^6$	0	5535.98
(R2)	$\text{C}_{\text{soot-H}} + \text{OH} \rightleftharpoons \text{C}_{\text{soot}^\circ} + \text{H}_2\text{O}$	f	$10^4$	0.734	719.68
		r	$3.68 \times 10^2$	1.139	8605.94
(R3)	$\text{C}_{\text{soot}^\circ} + \text{H} \longrightarrow \text{C}_{\text{soot}} + \text{H}_2\text{O}$	f	$10^4$	0.734	719.68
(R4)	$\text{C}_{\text{soot}^\circ} + \text{C}_2\text{H}_2 \longrightarrow \text{C}_{\text{soot-H}}$	f	80	1.56	1912.43
(R5)	$\text{C}_{\text{soot}^\circ} + \text{O}_2 \longrightarrow 2\text{CO}$	f	$2.2 \times 10^6$	0	3774.53
(R6)	$\text{C}_{\text{soot-H}} + \text{OH} \longrightarrow \text{CO} + \frac{1}{2}\text{H}_2$	f	$1.3 \times 10^7$	0	0

The carbons on the surface of soot are oxidized via reaction with  $\text{O}_2$  and  $\text{OH}$  which decreases total carbon of soot and releases  $\text{CO}$  and  $\text{H}_2$  to gas mixture. The oxidation process is described by HACA mechanism.  $\text{O}_2$  and  $\text{OH}$  oxidation rates are calculated as

$$\omega_{ox,O_2}^i = \alpha^i k_{f5} [\text{O}_2] [C_{\text{soot}^\circ}^i], \quad (87)$$

$$\omega_{ox,OH}^i = \alpha^i k_{f6} [\text{OH}] [\text{soot}^i]. \quad (88)$$

The oxidation source term is calculated considering the number of carbon atoms removed from soot through each oxidation pathway by

$$I_{C_{tot},ox}^i = -(2\omega_{ox,O_2}^i + \omega_{ox,OH}^i) / \rho, \quad (89)$$

We assume that oxidation does not change the number of surface hydrogen atoms. The rate change of concentration of  $\text{CO}$ ,  $\text{H}$  and  $\text{OH}$  by oxidation is calculates as:

$$\left(\frac{d[\text{CO}]}{dt}\right)_{ox} = \sum_{i=1}^{n_{sec}} \omega_{ox,O_2}^i. \quad (90)$$

$$\left(\frac{d[\text{O}_2]}{dt}\right)_{ox} = - \sum_{i=1}^{n_{sec}} \omega_{ox,O_2}^i. \quad (91)$$

$$\left(\frac{d[\text{OH}]}{dt}\right)_{ox} = - \sum_{i=1}^{n_{sec}} \omega_{ox,OH}^i. \quad (92)$$

$$\left(\frac{d[\text{H}_2]}{dt}\right)_{ox} = \frac{1}{2} \sum_{i=1}^{n_{sec}} \omega_{ox,OH}^i. \quad (93)$$

## 5 PAH growth models

Here, four different PAH growth models are used to describe the conversion of PAHs to incipient particles and their adsorption on existing agglomerates. As mentioned before, the soot inception and

surface growth is not fully understood yet, but there is substantial evidence to support the collision of PAHs as a key step in inception and surface growth [107, 46, 108]. So, global inception models have been developed based PAH collision consisting of different pathways with single- or multi-step reactions. The collision frequency of gaseous species including PAH molecules and polymers depend on their mass and diameter, and it is obtained as:

$$\beta_{dim_{jk}} = 2.2 \cdot d_r^2 \sqrt{\frac{8\pi k_B T}{m_r}} \quad (94)$$

where  $d_r$  and  $m_r$  are reduced diameter and mass for two PAH molecules, respectively.

$$d_r = 2 \frac{d_{PAH_k} \cdot d_{PAH_j}}{d_{PAH_k} + d_{PAH_j}} \quad (95)$$

$$m_r = \frac{m_{PAH_k} \cdot m_{PAH_j}}{m_{PAH_k} + m_{PAH_j}} \quad (96)$$

The mass of each PAH molecule is obtained from its molecular weight as:

$$m_{PAH_j} = \frac{W_{PAH_j}}{Av} \quad (97)$$

The diameter of PAH is calculated from its mass and density.

$$d_{PAH_j} = \left( \frac{6 \cdot m_{PAH_j}}{\pi \cdot \rho_{PAH_j}} \right)^{1/3} \quad (98)$$

The density of a PAH molecule is estimated using the relation proposed by Johansson et al. [109].

$$\rho_{PAH_j} = 171943.5197 \frac{W_{carbon} \cdot n_{C,PAH_j} + W_{hydrogen} \cdot n_{H,PAH_j}}{n_{C,PAH_j} + n_{H,PAH_j}} \quad (99)$$

The collision frequency of  $PAH_j$  and soot agglomerates in each section can be determined for the entire regime by harmonic mean of the collision frequency in the free molecular and continuum regimes as:

$$\beta_{ads_j}^i = \frac{\beta_{fm,ads}^i \cdot \beta_{cont,ads}^i}{\beta_{fm,ads}^i + \beta_{cont,ads}^i} \quad (100)$$

$$\beta_{fm,ads_j}^i = 2.2 \sqrt{\frac{\pi k_B T}{2} \left( \frac{1}{m_{agg}^i} + \frac{1}{m_{PAH_j}} \right)} (d_g^i + d_{PAH_j})^2 \quad (101)$$

$$\beta_{cont,ads_j}^i = \frac{2k_B T}{3\mu} \left[ \frac{C^i(d_m)}{d_g^i} + \frac{C^i(d_{PAH_j})}{d_{PAH_j}} \right] (d_g + d_{PAH_j}) \quad (102)$$

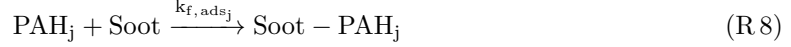
where  $C^i$  is the Cunningham function calculated as Equation 33.

## 5.1 Irreversible Dimerization

The irreversible dimerization is based on the irreversible collision of PAHs leading to their clustering/polymerization that forms dimers, trimers, and tetramers until the polymer mass reaches a threshold that can be considered a solid particle. For practical purposes, dimer is usually considered as a incipient particle that grows by surface growth and coagulation. A single-step irreversible collision of two similar PAHs forms a new dimer as:



Similarly, the adsorption of each PAH molecule on soot particles is described by the irreversible collision of soot and PAH<sub>j</sub> as:



The forward rate of dimerization,  $k_{f,dim_j}$  and adsorption,  $k_{f,ads_j}$  in Reactions (R 7) and (R 8) are calculated from Equations (94) and (100), respectively.

$$k_{f,dim_j} = \gamma_{inc} \cdot \beta_{jk,PAH} \cdot Av, \quad (103)$$

$$k_{f,ads_j}^i = \gamma_{ads_j} \cdot \beta_{j,ads}^i \cdot Av, \quad (104)$$

where  $\gamma_{inc}$  and  $\gamma_{ads}$  are the collision efficiencies for dimerization and adsorption, respectively. Their value vary in  $[10^{-7}, 1]$  range, and usually chosen to match the predicted soot mass with the experimental data. Here,  $\gamma_{inc} = 10^{-4}$  and  $\gamma_{ads} = 10^{-3}$ . The rate of dimerization and adsorption from PAH<sub>j</sub> are calculated accordingly as:

$$w_{dim_j} = \eta_{inc} k_{f,dim_j} [\text{PAH}_j] [\text{PAH}_j], \quad (105)$$

where  $\eta_{inc}$  is the inception adjustment factor to globally modify the inception flux without changing the internal rate constants of the inception model. The partial source terms for inception are calculated as:

$$I_{N,inc} = \frac{1}{\rho} \sum_{j=1}^{n_{PAH}} w_{dim_j} 2n_{PAH_j,C} \quad (106)$$

$$I_{C_{tot},inc} = \frac{1}{\rho} \sum_{j=1}^{n_{PAH}} w_{dim_j} 2n_{PAH_j,C} \quad (107)$$

$$I_{H_{tot},inc} = \frac{1}{\rho} \sum_{j=1}^{n_{PAH}} w_{dim_j} 2n_{PAH_j,H} \quad (108)$$

The rate of PAH adsorption for each section is obtained as:

$$w_{ads_j}^i = \eta_{ads} k_{f,ads_j}^i [\text{soot}] [\text{PAH}_j] \quad (109)$$

where  $\eta_{ads}$  is the adsorption adjustment factor to globally modify the PAH adsorption rate. The contribution of PAH adsorption to the source terms are expressed as:

$$I_{C_{tot},ads}^i = \frac{1}{\rho} \sum_{j=1}^{n_{PAH}} w_{ads_j}^i n_{PAH,C} \quad (110)$$

$$I_{H_{tot},ads}^i = \frac{1}{\rho} \sum_{j=1}^{n_{PAH}} w_{dim_j}^i (n_{PAH,H} - 2) \quad (111)$$

Each PAH molecule loses one H atom becoming a radical that forms bonds with a dehydrogenated site on soot surface, so two H atoms are released during the process that is taken into account in Equation (111).

The formation of a dimer consumes two PAH molecules, and during adsorption one PAH molecule is removed from the gas mixture, so the total rate of PAH<sub>i</sub> removal by the irreversible dimerization is obtained as:

$$\left( \frac{d[\text{PAH}_j]}{dt} \right)_{inc} = -2w_{dim_j} - \sum_{i=1}^{n_{sec}} w_{ads_j}^i. \quad (112)$$

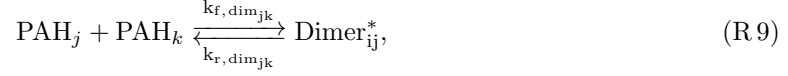
During the adsorption process one H<sub>2</sub> is released to the gas mixture.

$$\left( \frac{d[\text{H}_2]}{dt} \right)_{inc} = \sum_{i=1}^{n_{sec}} w_{ads_j}^i. \quad (113)$$



## 5.2 Reactive Dimerization

This model is built on Irreversible Dimerization with two main differences: The first step of dimerization and adsorption is reversible forming physically bonded dimers followed by a irreversible carbonization that leads to chemical bond formation in dimers [44]. This approach allows formation of homo- and heterodimers. The dimerization of PAH<sub>j</sub> and PAH<sub>k</sub> is described as:



where  $\text{Dimer}_{jk}^*$  and  $\text{Dimer}_{jk}$  physically and chemically bonded dimers, respectively, from PAH<sub>j</sub> and PAH<sub>k</sub>. The forward rate of physical dimerization,  $k_{f, \text{dim}_{jk}}$  is calculated from Equation (94) as:

$$k_{f, \text{dim}_{jk}} = p'' \cdot \beta_{jk, \text{PAH}} \cdot Av, \quad (114)$$

where  $p'' = 0.1$  accounts for the probability of PAH-PAH collisions in “FACE” configuration that results in successful vdW bond formation [110]. The reverse rate of physical dimerization,  $k_{r, \text{dim}_{jk}}$  is obtained from the dimerization equilibrium constant [40] as:

$$\log_{10} K_{eq} = a \frac{\epsilon_{jk}}{RT} + b, \quad (115)$$

$$k_{r, \text{dim}_{jk}} = k_{f, \text{dim}_{jk}} 10^{-b} e^{-a\epsilon_{jk} \ln(10)/(RT)}, \quad (116)$$

$$\epsilon_{jk} = cW_{jk} - d, \quad (117)$$

$$W_{jk} = \frac{W_j \cdot W_k}{W_j + W_k}, \quad (118)$$

where  $a = 0.115$  (obtained from pyrere dimerization data [35]) and  $b=1.8$  [44],  $c=933420$  j/kg, and  $d=34053$  j/mol [44].

The rate of chemical bond formation,  $k_{\text{reac}}$  is defined in the Arrhenius form [36] as

$$k_{\text{reac}} = 5 \times 10^6 \cdot e^{(-96232/RT)}. \quad (119)$$

Assuming a steady state condition for the physical dimers,  $\partial[\text{Dimer}_{jk}^*]/\partial t = 0$ , the rate of formation of chemically-bonded dimers can be obtained as

$$\omega_{\text{dim}_{jk}} = \eta_{\text{inc}} k_{\text{reac}} \frac{k_{f, \text{dim}_{jk}} [\text{PAH}_j] [\text{PAH}_k]}{k_{r, \text{dim}_{jk}} + k_{c, \text{dim}}}. \quad (120)$$

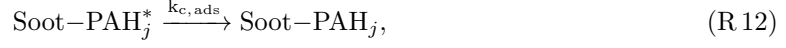
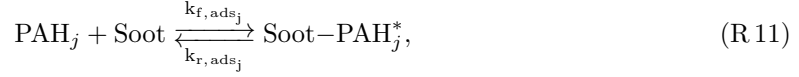
The contribution of dimer formation to partial source terms is expressed by looping over all combinations of PAHs as:

$$I_{N, \text{inc}} = \frac{1}{\rho} \sum_{j=1}^{n_{\text{PAH}}} \sum_{k=j}^{n_{\text{PAH}}} \omega_{\text{dim}_{kj}} (n_{\text{PAH}_j, C} + n_{\text{PAH}_k, C}), \quad (121)$$

$$I_{C_{\text{tot}}, \text{inc}} = \frac{1}{\rho} \sum_{j=1}^{n_{\text{PAH}}} \sum_{k=j}^{n_{\text{PAH}}} \omega_{\text{dim}_{kj}} (n_{\text{PAH}_j, C} + n_{\text{PAH}_k, C}), \quad (122)$$

$$I_{H_{\text{tot}}, \text{inc}} = \frac{1}{\rho} \sum_{j=1}^{n_{\text{PAH}}} \sum_{k=j}^{n_{\text{PAH}}} \omega_{\text{dim}_{kj}} (n_{\text{PAH}_j, H} + n_{\text{PAH}_k, H}), \quad (123)$$

Similarly, PAH adsorption is described by a two-step process where the collision of PAH<sub>j</sub> with soot agglomerates leads to physically bonded Soot – PAH\* that is carbonized and forms chemically-bonded Soot – PAH added to soot surface.



The forward rate of PAH-soot collision is calculated from Equation (100), and the reverse rate is determined same as inception (Equation(116)).

$$k_{f,ads}^i = \beta_{jk,ads}^i \cdot Av, \quad (124)$$

$$k_{r,ads}^i = k_{f,ads}^i \cdot 10^{-b} e^{-a\epsilon_{soot,j} \ln(10)/(RT)}, \quad (125)$$

$$\epsilon_{soot,j} = cW_{soot,j} - d, \quad (126)$$

a, b, c, d values are the same as those used in inception. Computing  $\epsilon_{soot,j}$  also requires "equivalent soot molecular weight",  $W_{soot}$  for section i, which is estimated from carbon mass of each agglomerate as:

$$W_{soot}^i = \frac{C_{tot}^i W_{carbon}}{N_{agg}^i} \quad (127)$$

The rate constant of carbonization of Soot – PAH<sub>j</sub>\* is defined as in the Arrhenius form similar to inception (Equation (119)). The prefactor is adjusted based on matching the numerical PSD [36] with measurements in the ethylene pyrolysis in a flow reactor [111].

$$k_{c,dim} = 2 \times 10^{10} \cdot e^{(-96232/RT)}. \quad (128)$$

The total adsorption rate can be calculated assuming a steady-state concentration for physically adsorbed PAH on soot,  $\partial[\text{Soot-PAH}^*]/\partial t = 0$  calculated in a similar way to inception flux (Equation (120)) as

$$\omega_{ads_j}^i = \eta_{ads} k_{c,ads} \frac{k_{f,ads_j} [\text{Soot}] [\text{PAH}_j]}{k_{r,ads_j} + k_{c,ads_j}}, \quad (129)$$

The contribution of PAH adsorption rate to partial source terms can be expressed as:

$$I_{C_{tot,ads}}^i = \frac{1}{\rho} \sum_{i=1}^{n_{PAH}} \omega_{ads_j}^i n_{C,PAH_j}, \quad (130)$$

$$I_{C_{tot,ads}}^i = \frac{1}{\rho} \sum_{i=1}^{n_{PAH}} \omega_{ads_j}^i (n_{H,PAH_j} - 2). \quad (131)$$

The rate of removal of PAH from gas mixture due to adsorption is given as

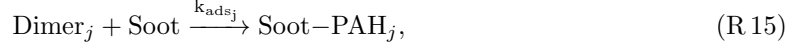
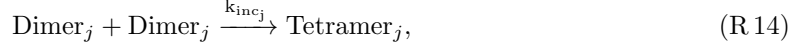
$$\left( \frac{d[\text{PAH}_j]}{dt} \right)_{inc} = - \sum_{k=1}^{n_{PAH}} w_{dim_{jk}} - \sum_{i=1}^{n_{sec}} w_{ads_j}^i. \quad (132)$$

During the adsorption process one H<sub>2</sub> is released to the gas mixture.

$$\left( \frac{d[\text{H}_2]}{dt} \right)_{inc} = \sum_{i=1}^{n_{sec}} w_{ads_j}^i. \quad (133)$$

### 5.3 Dimer Coalescence

Dimer coalescence model is a multi-step irreversible model proposed by Blanquart and Pitsch [76] where self-collision of PAH molecules form dimers that are intermediate state between gaseous PAH molecules and solid soot particles. The self-coalescence of dimers forms incipient soot particles. Alternatively, dimers can adsorb on the surface of existing soot particles and contribute to their surface growth. The equations are based on implementation of Dimer Coalescence by Sun et al. [112] for a sectional model.



where the rate constant of dimerization,  $k_{\text{dim}_j}$  and inception  $k_{\text{inc}_j}$  are calculated from collision rate of PAHs in Equation (100).

$$k_{\text{dim}_j} = \gamma_{\text{dim}_j} \cdot \beta_{jj, \text{PAH}} \cdot Av, \quad (134)$$

$$k_{\text{inc}_j} = \beta_{jj, \text{dimer}} \cdot Av, \quad (135)$$

where  $\gamma_{\text{dim}_j}$  is the dimerization efficiency that is assumed to scale with fourth power of PAH molecular weight [77] as:

$$\gamma_{\text{dim}_j} = C_{N,j} \cdot W_{\text{PAH}_j}^4, \quad (136)$$

Blanquart and Pitsch [76] estimated the constant  $C_{N,j}$  by comparing the profiles of several PAH species with experimental measurements in a single premixed benzene flame [113], and provided a efficiency values for various PAHs that are listed in Table 1 in [77]. The rate of dimer collision is expressed as:

$$w_{\text{dim}_j} = \eta_{\text{inc}} k_{\text{inc}_j} [\text{Dimer}_j] [\text{Dimer}_j] \quad (137)$$

Similarly, the rate of adsorption of dimers on soot particles is obtained as:

$$w_{\text{ads}_j}^i = \eta_{\text{ads}} k_{\text{ads}_j}^i [\text{soot}]^i [\text{Dimer}_j] \quad (138)$$

Assuming fast dimer consumption leads to the steady-state concentration of dimers that can be determined by solving a quadratic equation as:

$$a_{\text{inc}_j} [\text{dimer}]^2 + b_{\text{ads}_j} [\text{dimer}] = \omega_{\text{dim}_j} \quad (139)$$

$$[\text{Dimer}_j] = \begin{cases} \frac{-b_{\text{ads}_j} + \sqrt{\Delta_j}}{2a_{\text{inc}_j}}, & \text{if } \Delta_j \geq 0 \\ 0 & \text{if } \Delta_j < 0 \end{cases} \quad (140)$$

$$\Delta_j = b_{\text{ads}_j}^2 - 4a_{\text{inc}_j} \omega_{\text{dim}_j} \quad (141)$$

where  $a_{\text{inc}_j} = k_{\text{inc}_j}$  and  $b_{\text{ads}_j}$  is calculated by summing the adsorption rate of dimer for all sections and dividing it by the dimer concentration.

$$b_{\text{ads}_j} = \sum_{i=1}^{n_{\text{sec}}} k_{\text{ads}_j}^i [\text{soot}]^i \quad (142)$$

After determining the concentration of each dimer, the contribution of inception and PAH adsorption to source terms of tracked soot variables can be calculated similar to previous inception models considering the number of carbon and hydrogen atoms involved in the process.

$$I_{N,inc} = \frac{1}{\rho} \sum_{j=1}^{n_{PAH}} 4\omega_{inc_j} n_{PAH_j,C}, \quad (143)$$

$$I_{C_{tot},inc} = \frac{1}{\rho} \sum_{j=1}^{n_{PAH}} 4\omega_{inc_j} n_{PAH_j,C}, \quad (144)$$

$$I_{H_{tot},inc} = \frac{1}{\rho} \sum_{j=1}^{n_{PAH}} 4\omega_{inc_j} (n_{PAH_j,H} - 2), \quad (145)$$

$$I_{C_{tot},ads}^i = \frac{1}{\rho} \sum_{i=1}^{n_{PAH}} 2\omega_{ads_j}^i n_{C,PAH_j}, \quad (146)$$

$$I_{C_{tot},ads}^i = \frac{1}{\rho} \sum_{i=1}^{n_{PAH}} 2\omega_{ads_j}^i (n_{H,PAH_j} - 2). \quad (147)$$

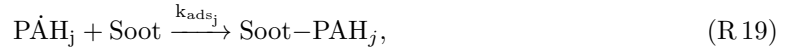
The rate of removal of PAHs and release of H<sub>2</sub> due to inception and PAH adsorption is calculated as:

$$\left( \frac{d[PAH_j]}{dt} \right)_{inc} = -4 \sum_{k=1}^{n_{PAH}} w_{inc_j} - 2 \sum_{i=1}^{n_{sec}} w_{ads_j}^i. \quad (148)$$

$$\left( \frac{d[H_2]}{dt} \right)_{inc} = 2 \sum_{i=1}^{n_{sec}} w_{ads_j}^i. \quad (149)$$

## 5.4 E-Bridge Formation

The E-Bridge Formation was originally proposed by Frenklach and Mebel [45] to describe soot inception using a HACA-like scheme that starts with dehydrogenation of PAH monomers, often pyrene, which forms the monomer radicals and continues with of sequential addition of the radicals to PAHs that form dimers, trimers and larger polymers until the PAH structure reaches the mass threshold and the clustering process becomes irreversible. Here, a modified version of EBridge Formation model is used where dimers are considered as incipient soot, and monomer radical are adsorbed on soot agglomerates. This PAH growth model is described using the following set of pathways:



The rate constants of Reactions (R 16)&(R 17) are listed in Table 3 while those of dimer production and adsorption are calculated based on Equations (94)&(100), respectively. For both steps, it is assumed the all collisions are successful i.e. 100% collision efficiency for radical-monomer and radical-soot.

$$k_{inc_j} = \beta_{jj,PAH} \cdot Av, \quad (150)$$

$$k_{ads_j}^i = \beta_{ads_j}^i \cdot Av, \quad (151)$$

Table 3: Rate coefficients for the monomer de-/hydrogenation reaction of E-bridge formation in Arrhenius form  $k = AT^n \cdot e^{-E/RT}$  [45]

Reaction		A $\left[\frac{\text{m}^3}{\text{mol}\cdot\text{s}}\right]$	n	$\frac{E}{R}[\text{K}]$
(R 16)	f	$98 \times n_{C,PAH_j}$	1.8	7,563.519
	r	$1.6 \times 10^{-2}$	2.63	2145.346
(R 17)	f	$4.8658 \times 10^7$	0.13	0.0

The rate of dimer formation and adsorption is calculated as:

$$w_{dim_j} = \eta_{inc} k_{inc_j} [PAH_j] [\dot{P}AH_j] \quad (152)$$

$$w_{ads_j}^i = \eta_{ads} k_{ads_j}^i [Soot]^i [\dot{P}AH_j] \quad (153)$$

The calculations of rate of inception and PAH adsorption from  $PAH_j$  requires the concentration of corresponding monomer radical that can be determined by applying the steady-state assumption for  $\dot{P}AH_j$ .

$$\begin{aligned} \frac{d[\dot{P}AH_j]}{dt} = 0 \\ k_{f,d_j} [PAH_j] [H] - k_{r,d_j} [\dot{P}AH_j] [H_2] - k_{f,h_j} [\dot{P}AH_j] [H] - k_{inc_j} [\dot{P}AH_j]^2 \\ - \sum_{i=1}^{n_{sec}} k_{ads_j}^i [\dot{P}AH_j] [Soot]^i = 0 \end{aligned}$$

The above equations can be rearranged as a quadratic equation similar to the dimer coalescence.

$$a_{inc_j} [\dot{P}AH_j]^2 + b_{ads_j} [\dot{P}AH_j] + c_j = 0, \quad (154)$$

$$a_{inc_j} = k_{f,d_j} \quad (155)$$

$$b_{ads_j} = k_{r,d_j} [H_2] + k_{f,h_j} [H] + \sum_{i=1}^{n_{sec}} k_{ads_j}^i [Soot]^i \quad (156)$$

$$c_{inc_j} = k_{f,d_j} [PAH_j] [H] \quad (157)$$

Finally, solving the quadratic equation for each PAH results in concentration of the radical using the following equation as:

$$[\dot{P}AH_j] = \begin{cases} \frac{-b_{ads_j} + \sqrt{\Delta_j}}{2a_{inc_j}}, & \text{if } \Delta_j \geq 0 \\ 0 & \text{if } \Delta_j < 0 \end{cases} \quad (158)$$

$$\Delta_j = b_{ads_j}^2 - 4a_{inc_j} c_j \quad (159)$$

The contribution of inception and adsorption to the partial source terms for E-Bridge formation can be written as:

$$I_{N,inc} = \frac{1}{\rho} \sum_{j=1}^{n_{PAH}} 2\omega_{inc_j} n_{PAH_j,C}, \quad (160)$$

$$I_{C_{tot},inc} = \frac{1}{\rho} \sum_{j=1}^{n_{PAH}} 2\omega_{inc_j} n_{PAH_j,C}, \quad (161)$$

$$I_{H_{tot},inc} = \frac{1}{\rho} \sum_{j=1}^{n_{PAH}} 2\omega_{inc_j} (n_{PAH_j,H} - 2), \quad (162)$$

$$I_{C_{tot},ads}^i = \frac{1}{\rho} \sum_{i=1}^{n_{PAH}} \omega_{ads_j}^i n_{C,PAH_j}, \quad (163)$$

$$I_{C_{tot},ads}^i = \frac{1}{\rho} \sum_{i=1}^{n_{PAH}} \omega_{ads_j}^i (n_{H,PAH_j} - 2). \quad (164)$$

The rate of removal of each PAH involved in soot inception and PAH adsorption and release of  $H_2$  to the gas mixture can be expressed as:

$$\left( \frac{d[PAH_j]}{dt} \right)_{inc} = -2 \sum_{k=1}^{n_{PAH}} w_{inc_k} - \sum_{i=1}^{n_{sec}} w_{ads_j}^i. \quad (165)$$

$$\left( \frac{d[H_2]}{dt} \right)_{inc} = \sum_{i=1}^{n_{sec}} w_{ads_j}^i. \quad (166)$$

## 6 Gas scrubbing rates

The rate of production/destruction of species involved in soot formation must be taken into account to preserve the mass and energy balance in reactive systems. In order to do that, the production rate of gaseous species calculated by Cantera must be corrected for the rate of release/consumption due to PAH growth and surface reaction models.

$$\left( \frac{d[PAH_j]}{dt} \right)_{tot} = \left( \frac{d[PAH_j]}{dt} \right)_{gas} + \left( \frac{d[PAH_j]}{dt} \right)_{inc} + \left( \frac{d[PAH_j]}{dt} \right)_{ads}. \quad (167)$$

$H_2$  is released to the gas mixture due to inception, PAH adsorption as well as oxidation.

$$\left( \frac{d[H_2]}{dt} \right)_{tot} = \left( \frac{d[H_2]}{dt} \right)_{gas} + \left( \frac{d[H_2]}{dt} \right)_{inc} + \left( \frac{d[H_2]}{dt} \right)_{ads} + \left( \frac{d[H_2]}{dt} \right)_{ox}. \quad (168)$$

Surface growth consumes  $C_2H_2$  and adds  $H_2$  to the gas mixture.

$$\left( \frac{d[C_2H_2]}{dt} \right)_{tot} = \left( \frac{d[C_2H_2]}{dt} \right)_{gas} + \left( \frac{d[C_2H_2]}{dt} \right)_{gr}. \quad (169)$$

$$\left( \frac{d[H]}{dt} \right)_{tot} = \left( \frac{d[H]}{dt} \right)_{gas} + \left( \frac{d[H]}{dt} \right)_{gr}. \quad (170)$$

Oxidation uses  $O_2$  and  $OH$  to remove carbon from soot particles and generates  $H_2$  and  $CO$ .

$$\left( \frac{d[CO]}{dt} \right)_{tot} = \left( \frac{d[CO]}{dt} \right)_{gas} + \left( \frac{d[CO]}{dt} \right)_{ox}. \quad (171)$$

$$\left( \frac{d[O_2]}{dt} \right)_{tot} = \left( \frac{d[O_2]}{dt} \right)_{gas} + \left( \frac{d[O_2]}{dt} \right)_{ox}. \quad (172)$$

$$\left( \frac{d[OH]}{dt} \right)_{tot} = \left( \frac{d[OH]}{dt} \right)_{gas} + \left( \frac{d[OH]}{dt} \right)_{ox}. \quad (173)$$

## 7 Code Validation

A set of simulations was performed to ensure the accuracy and reliability of omnisooot for prediction of soot formation. Aerosol dynamics is validated by comparing the results of population balance models implemented in omnisooot with those of DEM simulations from literature. Carbon and hydrogen mass and energy balance is also rigorously evaluated to ensure that residuals fall within the bounds of acceptable numerical error.

### 7.0.1 Collision Frequency

The collision frequency function determines the rate at which two particles collide, which results in the reduction of total number of agglomerates and increase in size. In the absence of strong flow shear or external forces, Brownian motion is the main driving force for particle coagulation. As explained in Sections 3.5.1 & 3.6.1, omnisooot employs harmonic mean and Fuchs interpolations to calculate collision frequency of agglomerates from free-molecular to continuum regimes based on gas mean free path, and particle morphology.

The test case for validation of collision frequency is based on the DEM simulation of 2000 monodisperse spherical particles with the density of  $2200 \text{ kg/m}^3$  in a cubic cell with the constant temperature of 298 K and pressure of 1 atm [114]. Figure 7 depicts the collision frequency plotted against Knudsen number ( $\text{Kn} = 2\lambda/d_m$ ) obtained by omnisooot using harmonic mean (red solid line) and Fuchs interpolation (green dashed line) and DEM results of Goudeli et al. [114]. The Fuchs interpretation perfectly matches DEM data over the free-molecular ( $\text{Kn} < 10$ ) to the continuum ( $\text{Kn} > 10$ ) range. Harmonic mean is also in good agreement with the DEM results in the free-molecular and continuum regime, but slightly underpredicts the collision frequency in the transition regime ( $0.1 \leq \text{Kn} \leq 10$ ) with relative errors less than 16%.

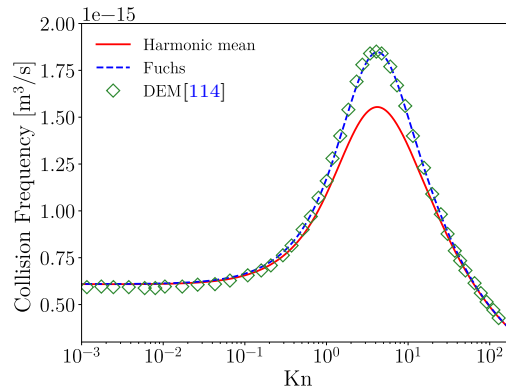


Figure 7: The comparison of collision frequency,  $\beta$ , obtained by omnisooot using harmonic mean (red solid line) and Fuchs interpolation (green dashed line) with DEM results (symbols) [114]

### 7.1 Coagulation

This test case was designed and conducted to validate the coagulation sub-unit of both particle dynamics models, MPBM and SPBM, by comparing the results of omnisooot with those of DEM [115]. The constant volume reactor was used for this test case, but it will be applicable to other reactors and flame models as long as the particle residence time matches with the values obtained by DEM. An adiabatic reactor with the volume of  $1 \text{ m}^3$  is initialized with  $2.6261 \times 10^{18}$  spherical particles 2 nm in diameter. The initial conditions are indicated in Table 4. The particles are allowed to coagulate in the free molecular regime and grow in size while no inception, PAH adsorption and surface growth occur. Figure 9 demonstrates the number density of agglomerates ( $N_{agg}$ ) and primary particles ( $N_{pri}$ ), and mobility ( $d_m$ ) and gyration ( $d_m$ ) diameters of particle obtained by omnisooot that are



Table 4: The simulations conditions of the coagulation test case [115]

Property	Value
Composition	CH <sub>4</sub> :0.425, O <sub>2</sub> :0.435, N <sub>2</sub> :0.14
T	1830 K
P	1 atm
$N_{agg}^1$	$3.514 \times 10^{-5}$ mol/kg
$N_{pri}^1$	$3.514 \times 10^{-5}$ mol/kg
$d_p^1$	2 nm

in good agreement with DEM results.  $N_{pri}$  is conserved during coagulation resulting in identical flat lines for both particle dynamics models, but  $N_{agg}$  declines over time with the higher decay rate for SPBM because it accounts for the polydispersity of agglomerates that results in larger collision frequency compared to MPBM. Therefore, mean mobility and gyration diameter of SPBM (red lines in Fig. 9-b) are slightly larger than those of MPBM (blue line of the same figure).

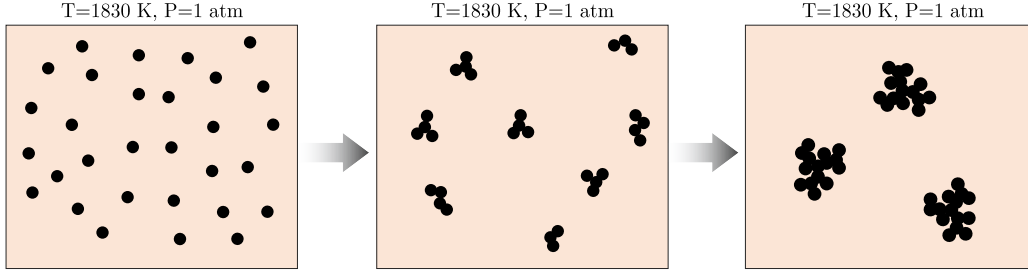


Figure 8: The schematic of agglomeration process in the coagulation test cases where initially spherical particle collide and form agglomerate

MPBM model cannot resolve PSD because of the monodispersity assumption. In contrast, SPBM tracks the number concentration of particles in separate sections that can be used to construct evolving PSD and calculate mean properties and determine the spread of size distribution of particles during coagulation. Figure 10-a shows the standard deviation of mobility diameter,  $\sigma_g$  predicted by SPBM in close agreement with DEM results.  $\sigma_g$  starts from unity indicating a monodisperse population at the beginning of simulation, and it finally reaches 2.03 that is the signature standard deviation of the free molecular regime [116]. Fig. 10 demonstrates the evolution of non-dimensional PSD from  $t=1$  ms to 677 ms. The PSD is plotted for the normalized concentration,  $\Psi = \bar{v}n_{agg}(v, t)/N_{agg,inf}$  and dimensionless volume,  $\eta = v/\bar{v}$ , where  $n_{agg}(v, t)$  is the size distribution function of agglomerate,  $v$  particle volume,  $\bar{v}$  mean particle volume,  $N_{agg,inf}$  total number concentration of agglomerates. For short residence times,  $t \approx 4$  ms, the PSD resembles a half bell curve because the majority of particles has sizes close to  $d_0 = 2$  nm with the average volume close to the minimum volume, so the particles with  $\eta \approx 1$  has the largest concentration. As particles grow by coagulation, the PSD rapidly transitions to a full bell-curve ( $t \geq 22$  ms) and does not change for longer residence times,  $t \geq 447$  ms marking the attainment of SPSD in a good agreement with DEM results. This confirms the capability of SPBM implemented in omnisoot to capture SPSD for soot agglomerates as a signature of Brownian-driven particle coagulation.

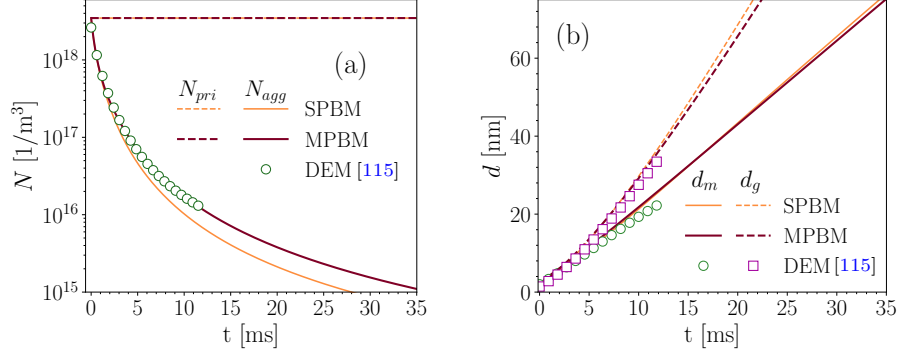


Figure 9: The total number concentration of agglomerates and primary particles (a), and mobility and gyration diameter (b) obtained with omnisoot using MPBM and SPBM that are in close agreement with the DEM results [115] indicating the validation of coagulation sub-model

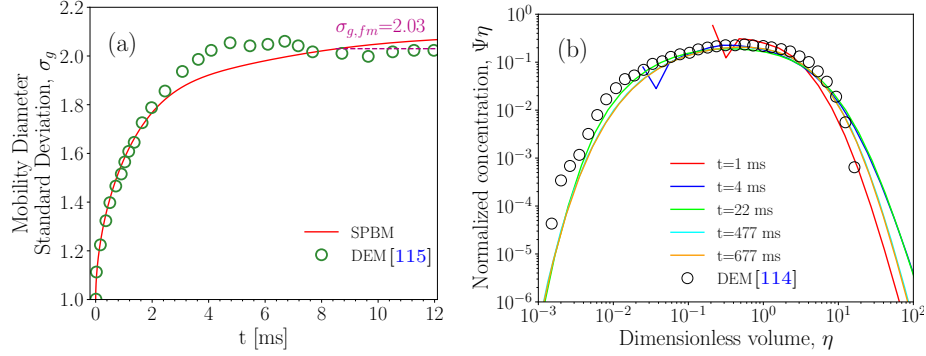


Figure 10: The standard deviation (residual) of mobility diameter,  $\sigma_g$  obtained with SPBM in close agreement with DEM results [115] (left pane) that reaches  $\sigma_{g, fm} = 2.03$  characteristic of the free molecular regime [116]; the particle size distribution (normalized number concentration of agglomerates is plotted against non-dimensional volume in the right pane) at different residence times that overlaps after initial transient phase marking the attainment of self-preserving size distribution in good agreement with DEM results [114]

## 7.2 Constant Volume Reactor

The pyrolysis of 30%  $\text{CH}_4$  diluted in  $\text{N}_2$  with the initial temperature and pressure of 2455 K and 3.47 atm, respectively, was simulated using the constant volume reactor model in the residence time of 40 ms. The combination of available PAH growth and particle dynamics models leads to eight different cases that were simulated to ensure the conservation of mass and energy. Here, we focus on the total elemental balance of carbon and hydrogen because they are involved in soot processes. Figure 11 demonstrates the relative error of total carbon, hydrogen and energy of system for different PAH growth and particle dynamics models in the constant volume that falls below  $10^{-10}$  for all parameters confirming the validity of model in satisfying the mass and energy balance in the constant volume reactor using all models.

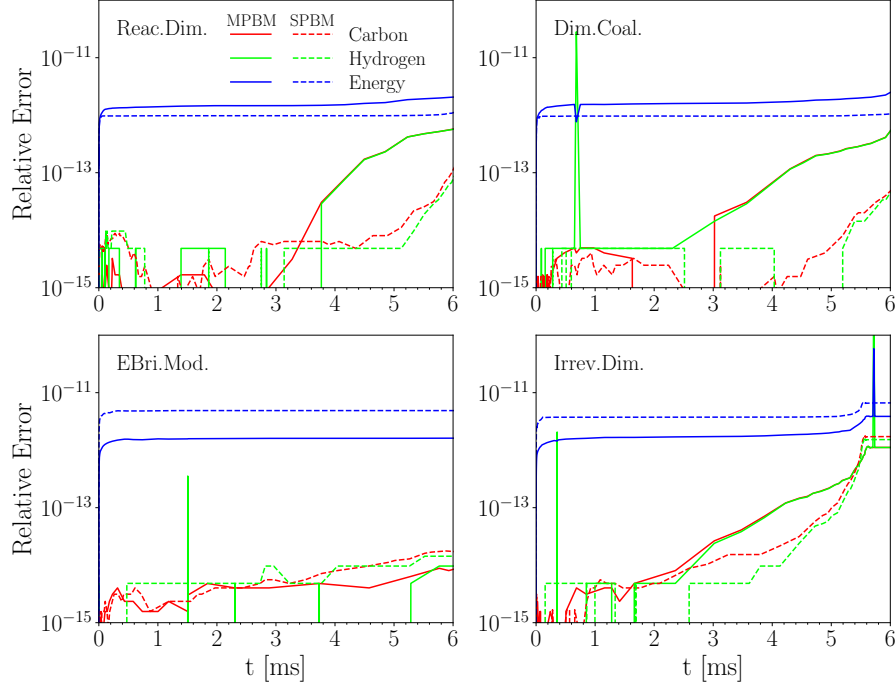


Figure 11: The relative error (residual) of total carbon (red line) and hydrogen (green line) mass, and total internal energy residual of gas and soot (blue line) plotted against residence time during pyrolysis of 30%  $\text{CH}_4\text{-N}_2$  at 2455 K and 3.47 atm in the constant volume reactor simulated using different PAH growth models along with MPBM (solid line) and SPBM (dashed line)

### 7.3 Constant Pressure Reactor

The pyrolysis of 5%  $\text{CH}_4\text{-Ar}$  in a shock-tube with post-reflected-shock temperature and pressure of  $T_5=2355$  K and  $P_5=4.64$  atm, respectively, was simulated using CPR model. Figure 12 shows the relative error of total carbon, hydrogen and energy of system for different PAH growth and particle dynamics models in the constant volume that falls below  $10^{-10}$  for all parameters confirming the validity of model in satisfying the mass and energy balance in the constant pressure reactor using all models.

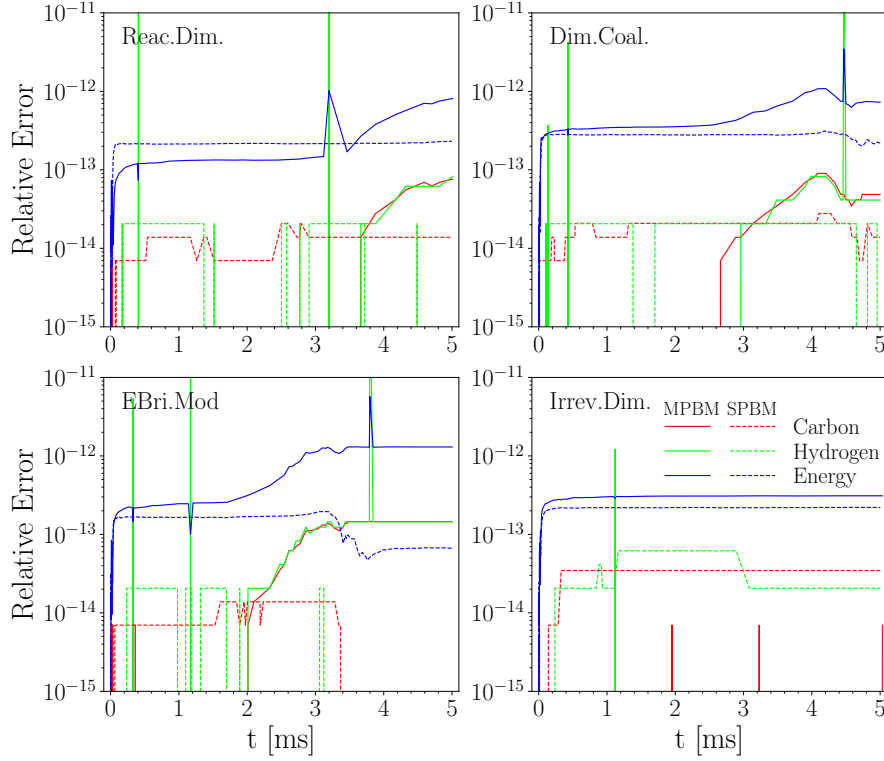


Figure 12: The relative error (residual) of total carbon (red line) and hydrogen (green line) mass, and total internal energy residual of gas and soot (blue line) plotted against residence time during pyrolysis of 5%  $\text{CH}_4$ -Ar at 2355 K and 4.64 atm simulated using the constant pressure reactor with different PAH growth model, MPBM (solid line) and SPBM (dashed line)

## 7.4 Plug Flow Reactor

Methane pyrolysis in an adiabatic flow reactor is used to check elemental carbon and hydrogen, and energy balance in the PFR model. The inlet flow enters the reactor at the composition of 30%  $\text{CH}_4$  diluted in  $\text{N}_2$ , and  $T=2100$  K and  $P=1$  atm. Figure 13 shows the residual of total elemental carbon and hydrogen, and energy up to 40 cm of the reactor length using all PAH growth and particle dynamics model. The residuals are in the order of  $10^{-11}$  and start to grow at the beginning of the reactor by pyrolysis of  $\text{CH}_4$  and the formation of intermediate species such as  $\text{C}_2\text{H}_2$  and PAHs. This initiates soot inception of surface growth affecting the gas chemistry and energy that ends near  $x=10$  cm, and then the coagulation of particles is dominant with no affect on mass and energy of particles. As a result, PFR model of omnisoot satisfied the conservation of the mass and energy.

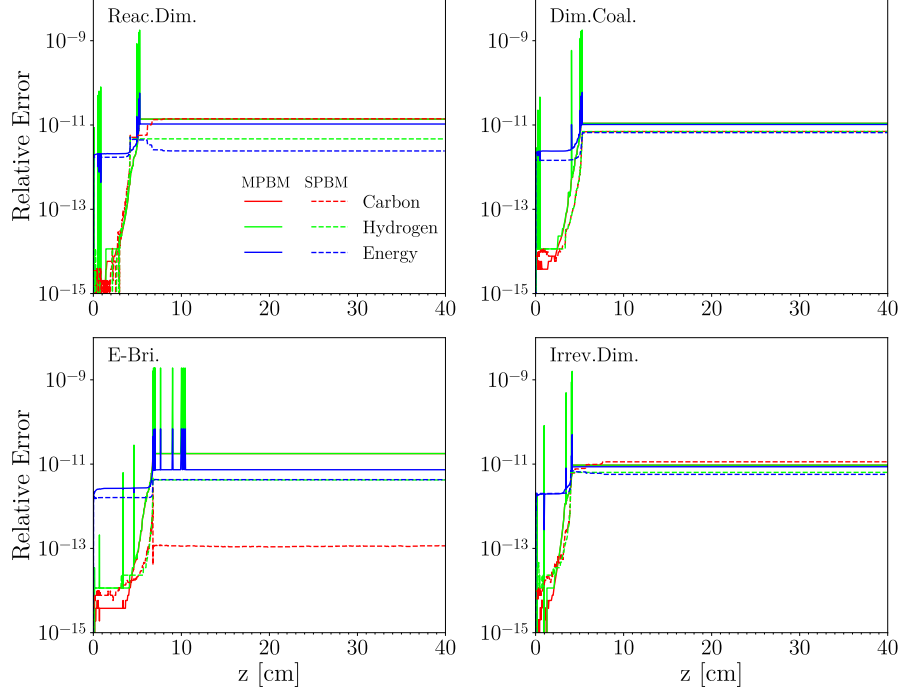


Figure 13: The relative error (residual) of total carbon (red line) and hydrogen (green line) mass, and total internal energy residual of gas and soot (blue line) plotted against reactor length (cm) in the adiabatic flow reactor during pyrolysis of 30% CH<sub>4</sub>-N<sub>2</sub> at 2100 K and 1 atm simulated using different PAH growth models and MPBM (solid line) and SPBM (dashed line)

## 7.5 Perfectly Stirred Reactor

The mass and energy balance are investigated for soot formation during ethylene-air oxidation at  $\phi = 2$  in a perfectly stirred reactor. The simulation conditions were chosen based on the combustor implemented and utilized by Stouffer et al. [117]. The reactants initially at 300 K enter a reactor of 250 ml that works under atmospheric pressure. The simulation is initialized from a high temperature (2000 K) to avoid trivial solution (cold reactant leaving the reactor with no chemical reactions) and to ensure the model captures a sustained combustion. The residence time of products in the reactor is 8.5 ms. Figure 14 shows the relative error of total elemental carbon and hydrogen mass and total enthalpy of gas and soot, which is less than  $10^{-6}$  for all combinations of particle dynamics and PAH growth models.

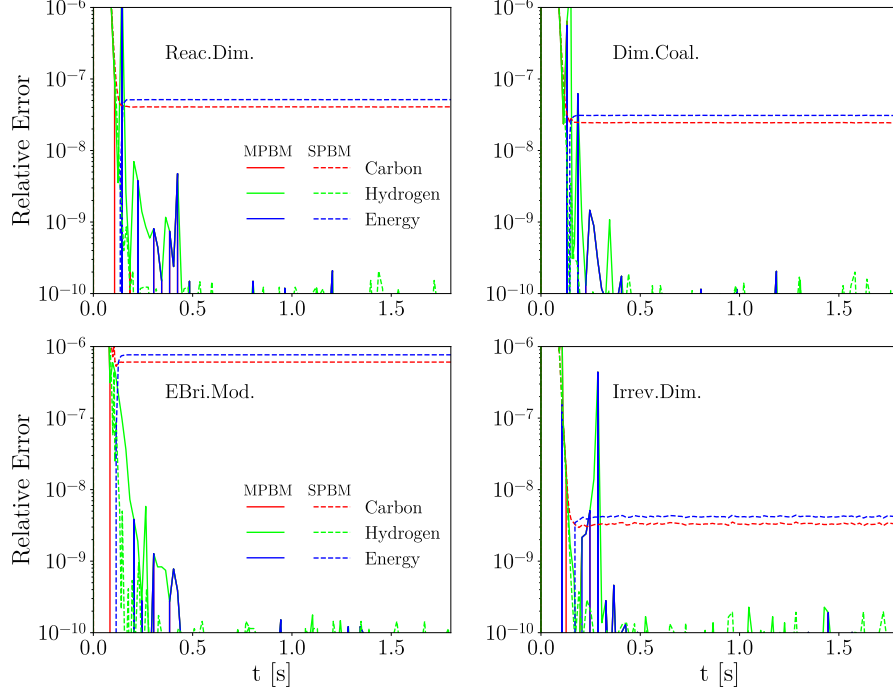


Figure 14: The relative error (residual) of total carbon (red line) and hydrogen (green line) mass, and total internal energy residual of gas and soot (blue line) plotted in simulation time during adiabatic combustion of  $C_2H_4$ -air with  $\phi = 2.1$  atm simulated using different PAH growth models and MPBM (solid line) and SPBM (dashed line)

## 8 Results and Discussion

### 8.1 Methane pyrolysis in shock-tube using constant pressure reactor

The pyrolysis of 5% and 10%  $CH_4$ -Ar was investigated using a constant pressure reactor model (CPR) for the post-shock temperature,  $T_5$  range of 1800-3000 K, and pressure,  $P_5$  range of 4.7-7.1 bar.  $P_5$  was not specified for each experiment (characterized with  $T_5$ ), so we assume that  $P_5$  linearly increases with  $T_5$ . Caltech mechanism was used to describe gas chemistry. The inception and PAH adsorption rates were adjusted using  $\eta_{inc}$  and  $\eta_{ads}$ , respectively to match the predicted carbon yield at  $t=1.5$  ms over the studied  $T_5$  and  $P_5$  with the extinction measurements at  $\lambda=632$  nm [118]. The measured carbon yield was retrieved from the reported  $yield \times E(m)$  considering the maximum variability in the absorption function of soot from 0.174 [119] to 0.37 [120] in the literature. Both adjustment factors were varied between 0 and 1, and Our parametric studies showed that there is not a

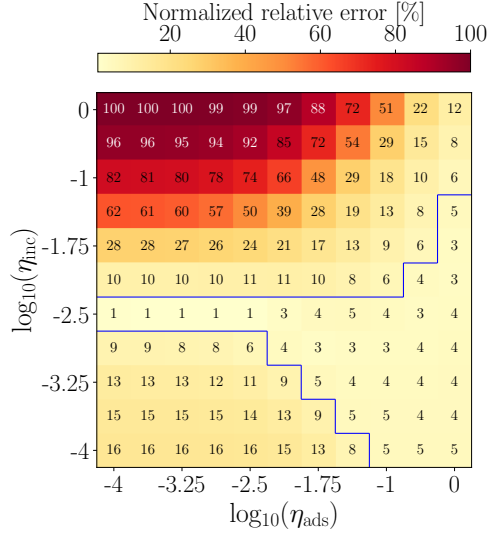


Figure 15: The relative error of carbon yield normalized by the maximum value at  $t=1.5$  ms for 5%  $\text{CH}_4$  obtained using Caltech mechanism and Reactive Dimerization

First, the model was run without soot (only the gas phase is simulated and no soot conversion allowed) to provide insight into the effect of temperature on the species involved in soot formation. Fig. ??-a shows the carbon mass fraction (CMF) of soot precursors at 1.5 ms that exhibits a bell-shape behavior reaching 7 and 12% of total carbon mass for 5 and 10%  $\text{CH}_4$ , respectively. The temperature of the peak CMF is 2350 K for 10%  $\text{CH}_4$  higher than that of 5%  $\text{CH}_4$  2125 K. On the other hand, the CMF of  $\text{C}_2\text{H}_2$  at 1.5 ms, shown in Fig. 16-b, increases linearly with temperature and then levels off. While doubling the initial  $\text{CH}_4$  mole fraction increases the peak CMF of precursors by nearly a factor of two, the maximum CMF of  $\text{C}_2\text{H}_2$  is nearly 0.85 for both cases.

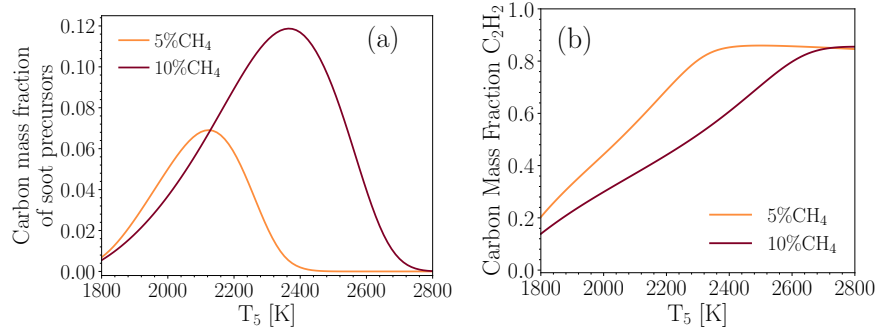


Figure 16: The bell-shape temperature profile of carbon mass fraction of soot precursors (A2 and larger) combined (a) and  $\text{C}_2\text{H}_2$  (b) at  $t=1.5$  ms during pyrolysis of 5% (red line) and 10%  $\text{CH}_4$ -Ar (green line) obtained using CPR model with Caltech mechanism without considering soot

Next set of simulations were conducted by using equal adjustment factor ( $\eta_{inc} = \eta_{ads}$ ) to minimize prediction error of mean soot carbon yield Fig. 17 compares soot carbon yield predicted using the different inception models and the sectional population balance model with the data from extinction measurements [118]. A skew exponential curve (represented by the black dotted line) was fitted to the data to highlight the trend in carbon yield, and its likely peak, which increases with initial



methane mole fraction from 12 to 32%. Soot carbon yield has a bell-shape profile similar to the one shown for soot precursor because soot inception flux and mass growth are directly tied to the concentration of precursors. All the inception models capture of the expected trend. As shown in Fig. 17-a, the agreement between the predicted carbon yield and the measurements are better for %5 CH<sub>4</sub> especially in T<sub>5</sub>2400 K. The yield predicted by Reactive Dimerization at T<sub>5</sub> less than the temperature of the peak yield is slightly larger than the other inception models. EBridge Modified seems to shifted to higher temperatures compared to other inception models indicating different temperature dependence of this model (PAH dehydrogenation) is described with an Arrhenius rate as opposed to the other model where inception is initiated with physical collision of PAHs.

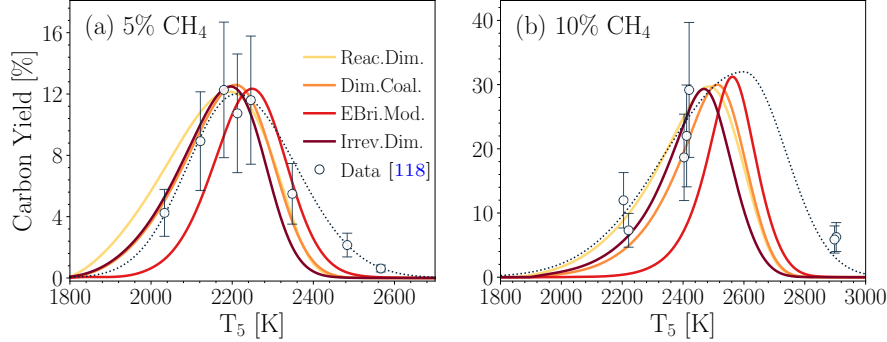


Figure 17: The bell-shape temperature profile of soot carbon yield at  $t=1.5$  ms for 5% (a) and 10% CH<sub>4</sub> (b) in Ar obtained using Caltech mechanism and different inception models calibrated to minimize the prediction with extinction measurements [118]. The dashed line was added to show the trend in the measurements.

As shown in Fig.18, the predicted  $d_p$  increases with T<sub>5</sub> over the studied temperature range. The differences between inception models is overall negligible except for Reactive Dimerization, which predicts a larger  $d_p$  compared to other inception models in T<sub>5</sub> range lower than 2500 and 2700 K for 5% and 10% CH<sub>4</sub>, respectively. As shown in Eq.(24),  $d_p$  is proportional of the third-root of  $C_{tot}/N_{pri}$ .  $C_{tot}$  describes total carbon mass converted to soot through inception and surface growth while  $N_{pri}$  is only determined by inception flux. As a result,  $d_p$  is controlled by the ratio of surface growth (HACA and PAH adsorption) rate to inception flux. To better understand this, the ratio of carbon mass gained by each pathway to the total soot carbon mass at 1.5 ms is calculated and shown in Fig.19. In the low temperature range, T<sub>5</sub> <2000 K, Reactive Dimerization directs the majority of the converted carbon to HACA and PAH adsorption (see Fig.19-a,b) resulting in larger  $C_{tot}/N_{pri}$  compared to other inception models that corresponds to larger  $d_p$  values. The carbon mass fraction of inception decreases with temperature for all inception models leading to increasing  $d_p$ .

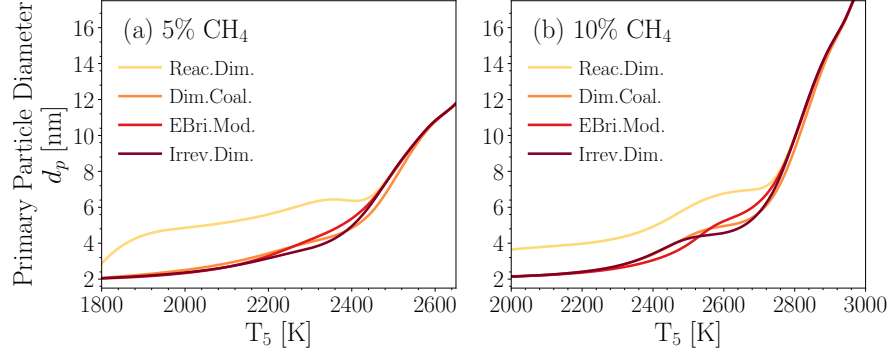


Figure 18: The temperature dependence of mean primary particle diameter,  $d_p$  at  $t=1.5$  ms for 5% (a) and 10%  $\text{CH}_4$  (b) in Ar obtained using Caltech mechanism and different inception models calibrated to minimize the prediction with extinction measurements [118].

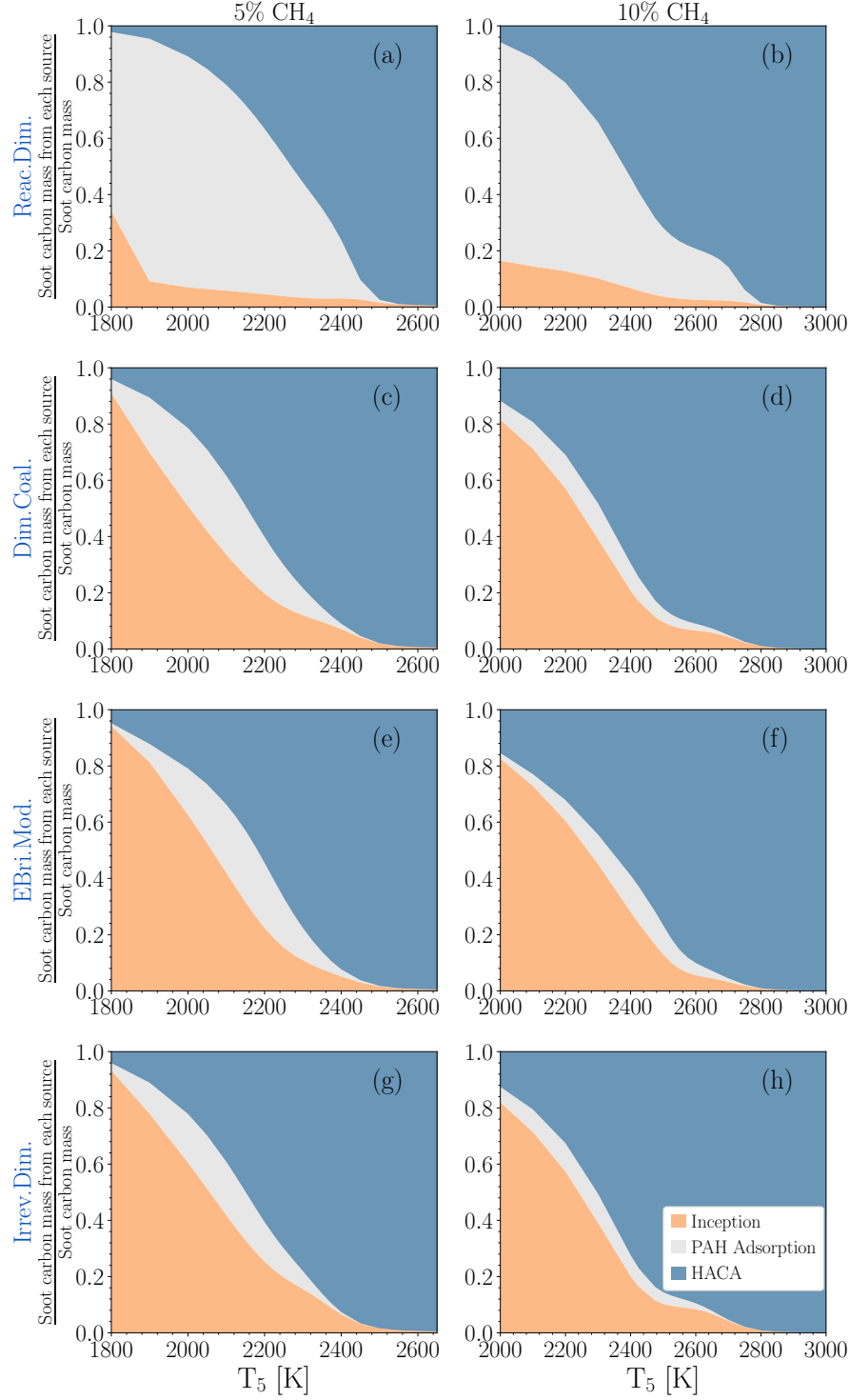


Figure 19: The soot carbon mass from inception, PAH adsorption and HACA normalized by total soot carbon mass at  $t=1.5$  ms for 5% (a) and 10%  $\text{CH}_4$  (b) in Ar obtained using Caltech mechanism and different inception models calibrated to minimize the prediction with extinction measurements [118].

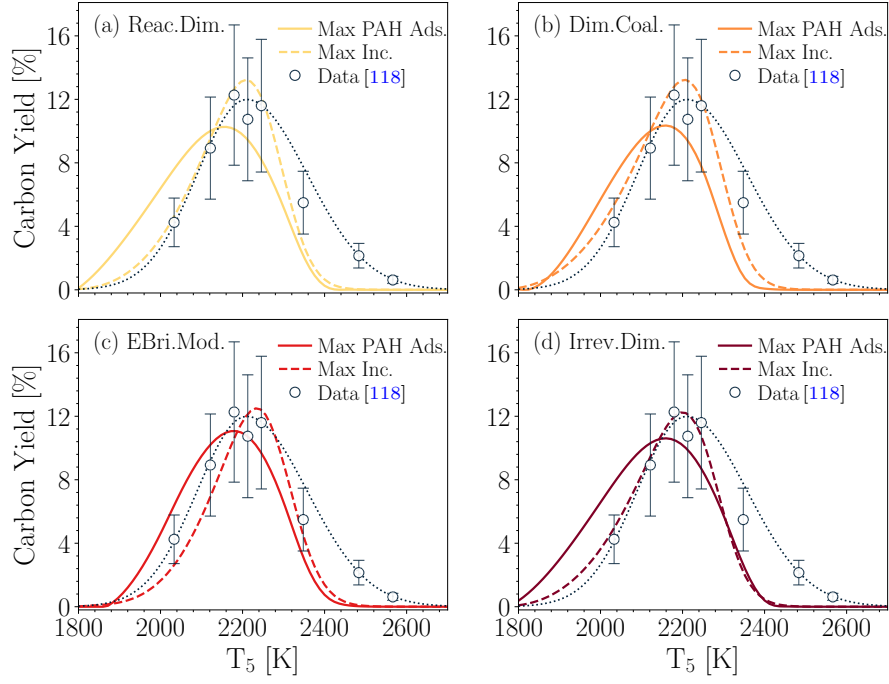


Figure 20: The comparison of soot carbon yield at  $t=1.5$  ms when maximum inception (dashed line) and PAH adsorption (solid line) were applied to minimized the prediction error compared to measurements [118] for 5% (a) and 10%  $\text{CH}_4$  (b) in Ar obtained using Caltech mechanism and different inception models.

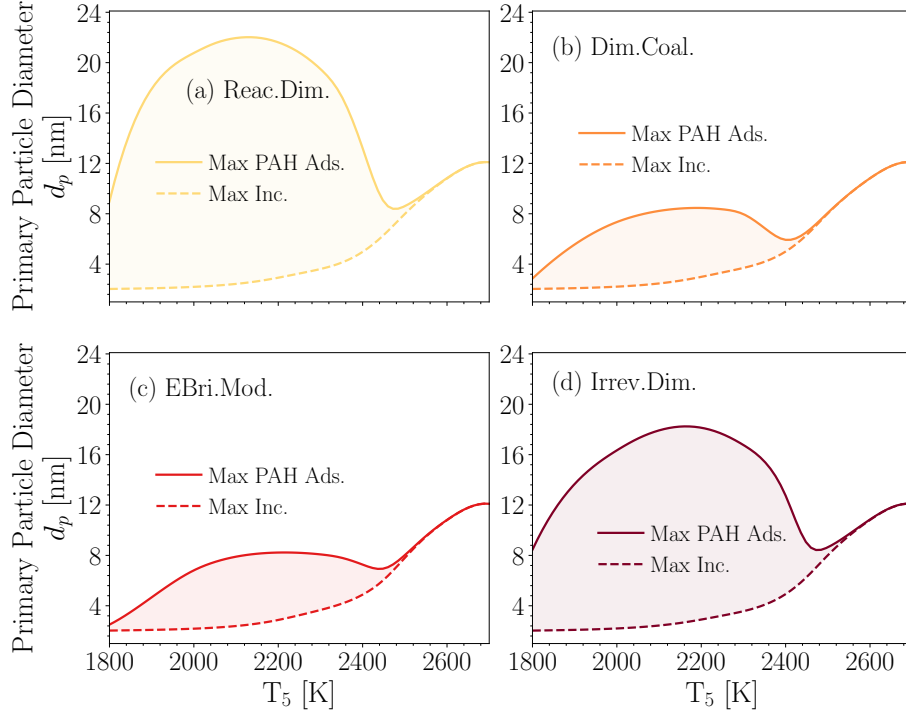


Figure 21: The comparison of mean primary particle,  $d_p$  at  $t=1.5$  ms when maximum inception and PAH adsorption were applied to minimized the prediction error compared to measurements [118] for 5% (a) and 10%  $\text{CH}_4$  (b) in Ar obtained using Caltech mechanism and different inception models.

## 8.2 Methane pyrolysis in shock-tube using constant volume reactor

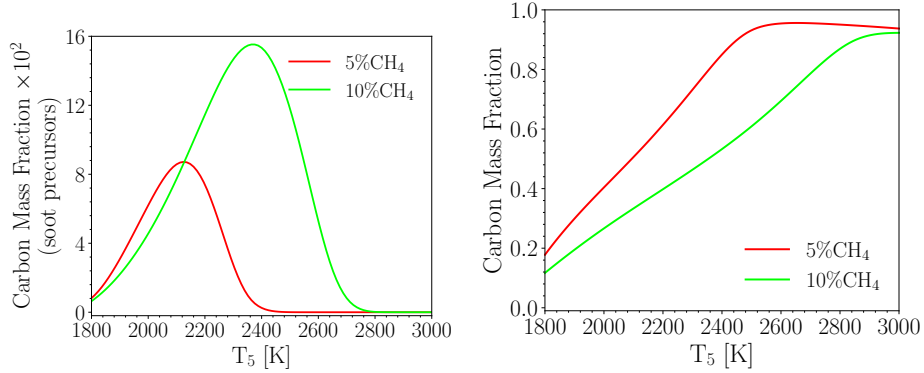


Figure 22: The bell-shape temperature profile of carbon mass fraction of soot precursors (A2 and larger) combined (a) and  $\text{C}_2\text{H}_2$  (b) at  $t=1.5$  ms during pyrolysis of 5% (red line) and 10%  $\text{CH}_4$ -Ar (green line) obtained using Caltech mechanism without considering soot

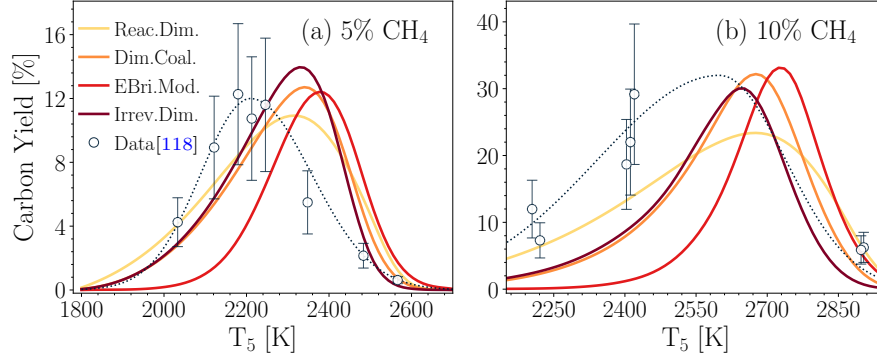


Figure 23: The bell-shape temperature profile of soot carbon yield at  $t=1.5$  ms for 5% (a) and 10%  $\text{CH}_4$  (b) in Ar obtained using Caltech mechanism and different inception models calibrated to minimize the prediction with extinction measurements [118].

Fig. ?? shows soot carbon yield predicted using Caltech mechanism where inception flux and PAH adsorption rate were adjusted using a scaling factor (equal for the both) to minimize the prediction error compared to the data from extinction measurements [118]. A skew exponential curve fit (represented by the black dotted line) was applied to illustrate the trend in soot yield and identify the temperature at which the yield likely reaches its maximum. The predicted temperature of peak yield is larger than peak of curve-fit in both  $\text{CH}_4$  concentrations by 100-200 K depending on the inception model. This difference is due the contribution of HACA to surface growth that depends on  $\text{C}_2\text{H}_2$  concentration which increases with temperature.

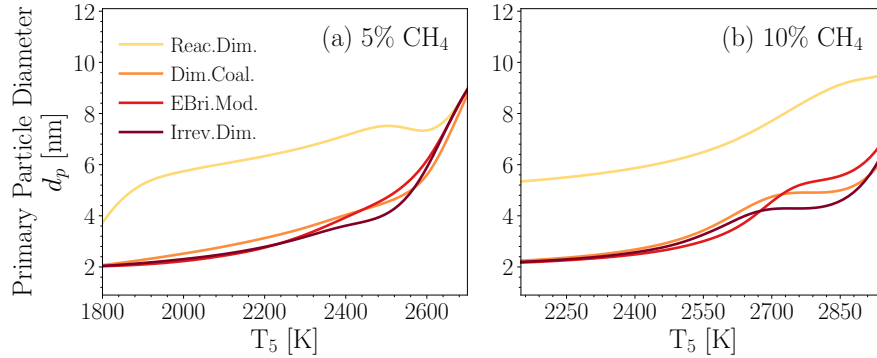


Figure 24: The temperature dependence of mean primary particle diameter,  $d_p$  at  $t=1.5$  ms for 5% (a) and 10%  $\text{CH}_4$  (b) in Ar obtained using Caltech mechanism and different inception models calibrated to minimize the prediction with extinction measurements [118].

Fig.?? shows that  $d_p$  increases with temperature up to 10 nm. For 5%  $\text{CH}_4$ ,  $d_p$  reaches the peak around 2800 K and drops quickly to 2 nm which is the minimum allowed diameter in the model. Reactive Dimerization results in overall larger primary particle diameters, but the behavior of the rest of inception models are similar.

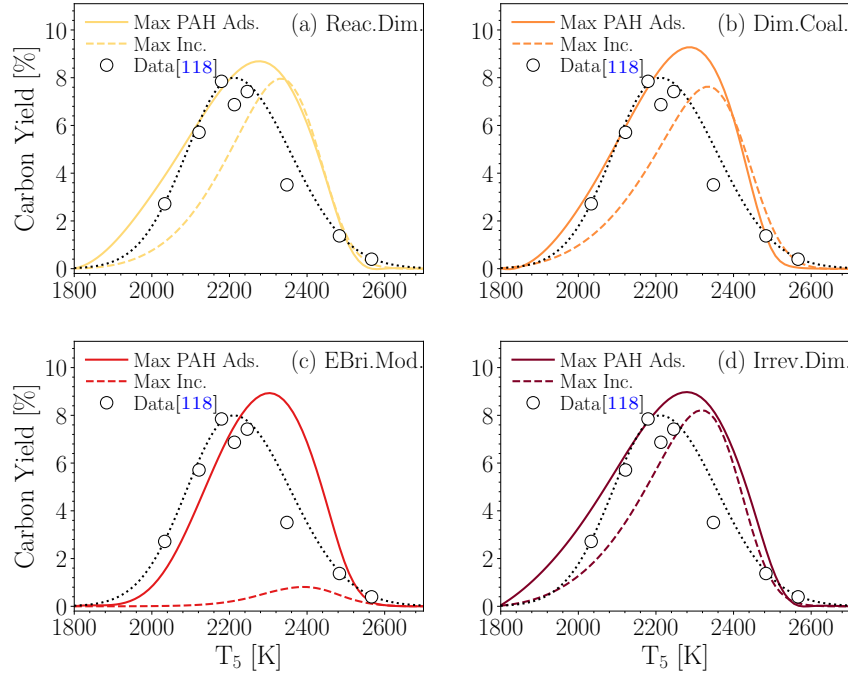


Figure 25: The comparison of soot carbon yield at  $t=1.5$  ms when maximum inception and PAH adsorption were applied to minimized the prediction error compared to measurements [118] for 5% (a) and 10%  $\text{CH}_4$  (b) in Ar obtained using Caltech mechanism and different inception models.

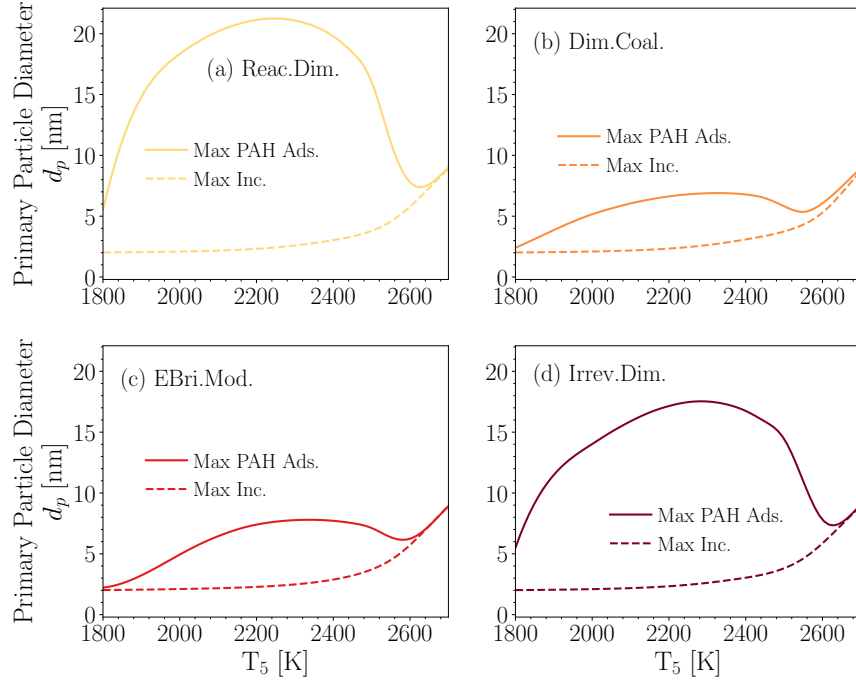


Figure 26: The comparison of mean primary particle,  $d_p$  at  $t=1.5$  ms when maximum inception and PAH adsorption were applied to minimized the prediction error compared to measurements [118] for 5% (a) and 10%  $\text{CH}_4$  (b) in Ar obtained using Caltech mechanism and different inception models.

### 8.3 Ethylene oxidation in a partially-stirred reactor

Manzello et al. [121] utilized NIST well-stirred reactor (WSR) connected to a flow reactor to study soot formation during ethylene oxidation at equivalence ratios of 1.9, 2.0, and 2.1, and provided PSD measurements at the end of flow reactor using nano-differential mobility analyzer (Nano-DMA). The WSR has the same size of the reactor used by Manzello et al. [121] and explained in Sec.7.5. The flow reactor is 70 cm long with an inner diameter of 5.1 cm. A coupled PSR-PFR reactor model of omnisoot was used with the same dimensions to study gas chemistry and soot inception during the combustion and flow evolution in the device. The nominal residence time,  $\tau$  of flow in the PSR is 11 ms Manzello et al. [121]. The reactants are assumed to enter PSR at 300 K with an inlet mass flow rate,  $\dot{m}_{in} = \rho V / \tau$  where  $\rho$  was calculated at reactor temperature of 1723 K suggested by Lenhert and Manzello [122]. The PFR is assumed to be adiabatic. The calculated average axial velocity in the PFR is 14.5 m/s close to the values suggested by Manzello et al. [121]. KAUST mechanism was used to describe gas chemistry. A single set of inception and PAH adsorption scaling factors were employed for each PAH growth model to match, as closely as possible, the predicted PSD with the measurements across three  $\phi$ s. As shown in Fig.27, all inception model capture the peak number concentration and the uni-modal shape of the PSD, which indicates that particle inception has ceased, and coagulation has become dominant. As reported in Table 5, the geometric mean mobility diameter,  $d_{m,g}$  and the geometric mobility standard deviation,  $\sigma_{m,g}$  obtained using all inception models are in good agreement with the values calculated from the measured PSD [121]. As it can be seen in Fig.27-(a) & (b), the spread of predicted PSD is narrower than that of measurements for  $\phi=1.9$  and 2.1, which corresponds to under-prediction of  $\sigma_{m,g}$  for these equivalence ratios.



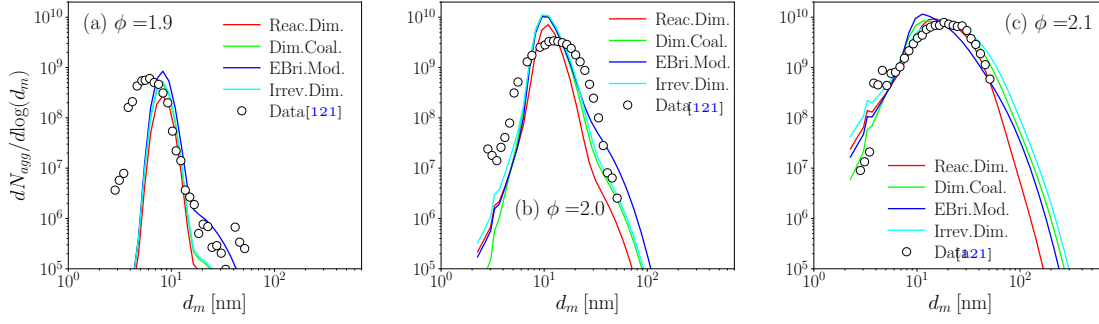


Figure 27: The particle size distribution at the end of PFR for  $\phi=1.9$  (a), 2.0 (b), and 2.1 (c) obtained using KAUST mechanism and different inception models calibrated to match the predictions with measurement [121].

Table 5: The geometric mean mobility diameter,  $d_{m,g}$ , and the geometric mobility standard deviation,  $\sigma_{m,g}$  obtained using different inception models compared with the value calculated from the measured PSD [121]

	$\phi = 1.9$		$\phi = 2.0$		$\phi = 2.1$	
	$d_{m,g}$ [nm]	$\sigma_{m,g}$	$d_{m,g}$ [nm]	$\sigma_{m,g}$	$d_{m,g}$ [nm]	$\sigma_{m,g}$
Data [121]	6.04	1.25	12.40	1.49	17.66	1.64
Reactive Dimerization	8.27	1.14	11.10	1.21	16.88	1.58
Dimer Coalescence	8.18	1.14	10.76	1.24	16.99	1.68
EBridge Modified	8.27	1.15	11.02	1.27	14.56	1.58
Irreversible Dimerization	8.19	1.14	10.96	1.25	18.44	1.78

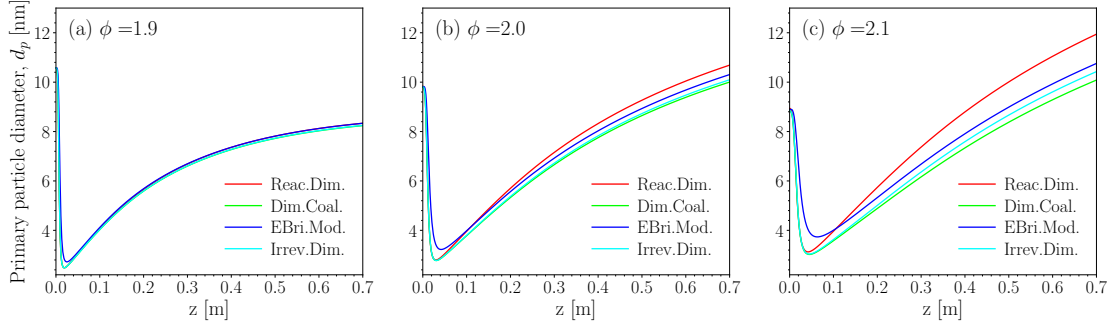


Figure 28: The primary particle diameter,  $d_p$  along the PFR for  $\phi=1.9$  (a), 2.0 (b), and 2.1 (c) obtained using KAUST mechanism and different inception models calibrated to match the predictions with measurement [121].

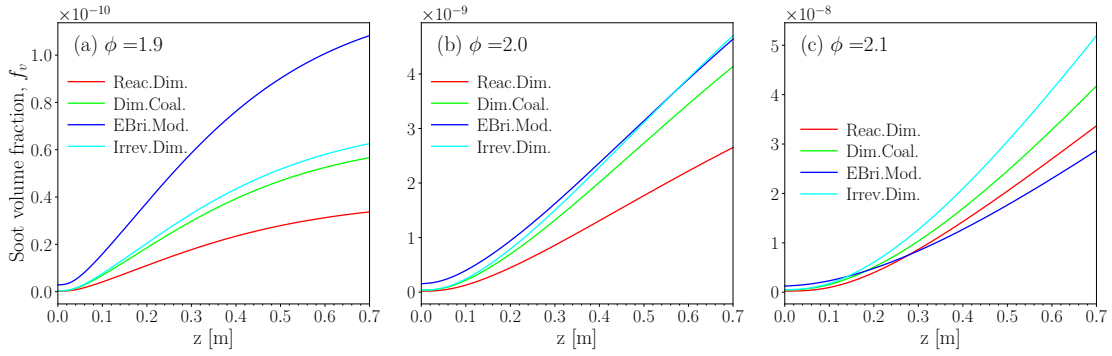


Figure 29: The soot volume fraction,  $f_v$  along the PFR for  $\phi=1.9$  (a), 2.0 (b), and 2.1 (c) obtained using KAUST mechanism and different inception models calibrated to match the predictions with measurement [121].

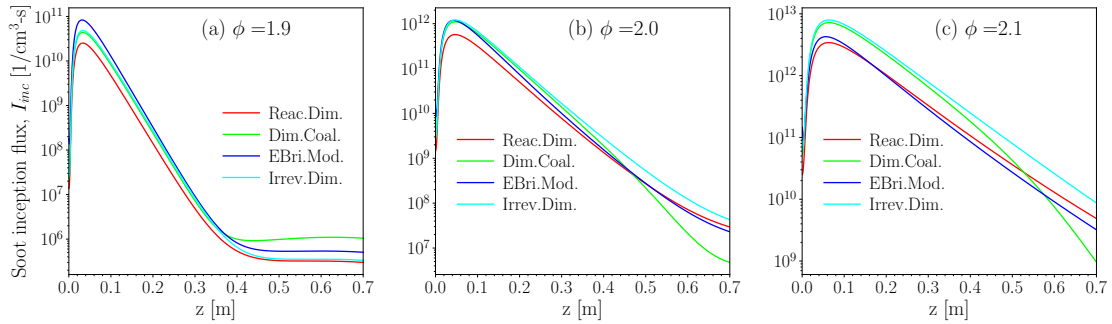


Figure 30: The soot inception flux,  $I_{inc}$  along the PFR for  $\phi=1.9$  (a), 2.0 (b), and 2.1 (c) obtained using KAUST mechanism and different inception models calibrated to match the predictions with measurement [121].

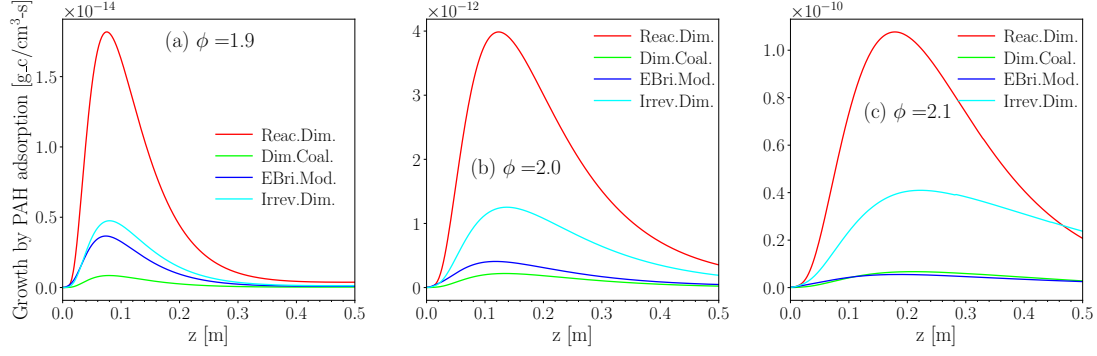


Figure 31: The carbon growth rate by PAH adsorption rate along the PFR for  $\phi=1.9$  (a), 2.0 (b), and 2.1 (c) obtained using KAUST mechanism and different inception models calibrated to match the predictions with measurement [121].

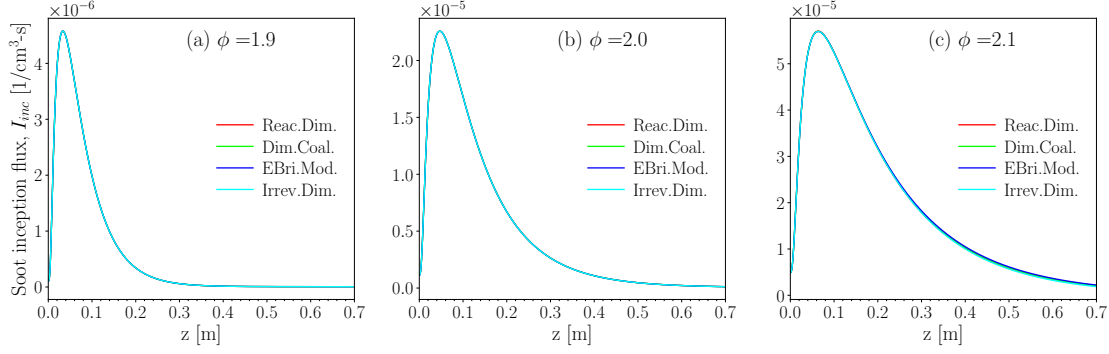


Figure 32: The mole fraction of acenaphthylene, A2R5 along the PFR for  $\phi=1.9$  (a), 2.0 (b), and 2.1 (c) obtained using KAUST mechanism and different inception models calibrated to match the predictions with measurement [121].

### 8.3.1 Ethylene pyrolysis in a flow reactor

The PFR model was used to simulate the pyrolysis of %0.6 C<sub>2</sub>H<sub>4</sub> – N<sub>2</sub> in a flow reactor 1.4 m long and 16 mm in diameter. The temperature profile was imposed in the model from the measurement along the reactor centerline by Mei et al. [123] for the maximum temperature of 1700 K. The inception and PAH adsorption scaling factors were used to match the predicted PSD with measurements at the volumetric flow rates, Q of 8.5, 11 and 12 L/min.

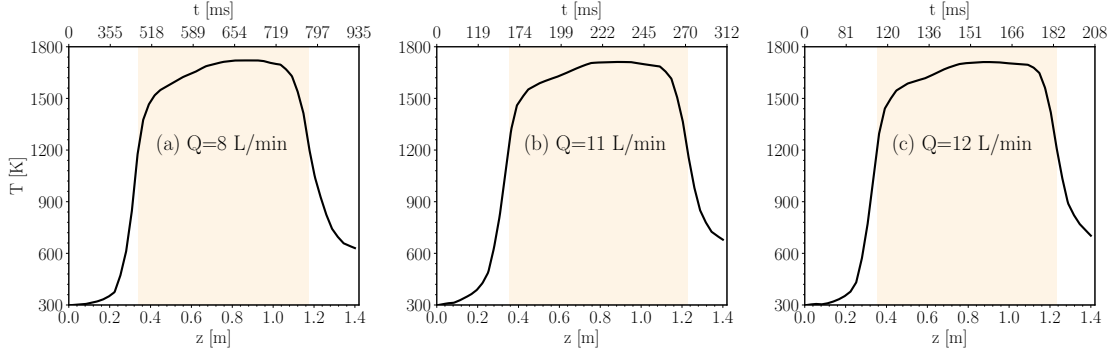


Figure 33: The centerline temperature along the reactor for  $Q=8$  (a), 11 (b), and 12 L/min (c) interpolated from the thermocouple measurements [123]. The yellow area represent the region with temperature larger than 1200 K.

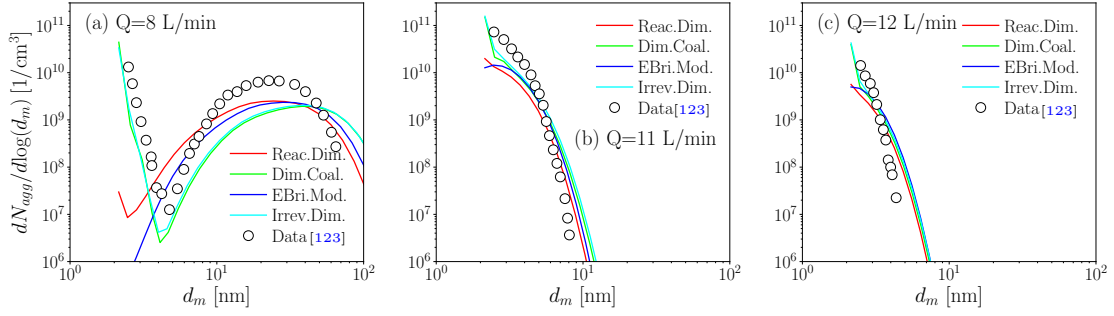


Figure 34: The particle size distribution at the end of PFR for  $Q=8.5$  (a), 11 (b), and 12 L/min (c) obtained using KAUST mechanism and different inception models calibrated to match the predictions with measurement [123].

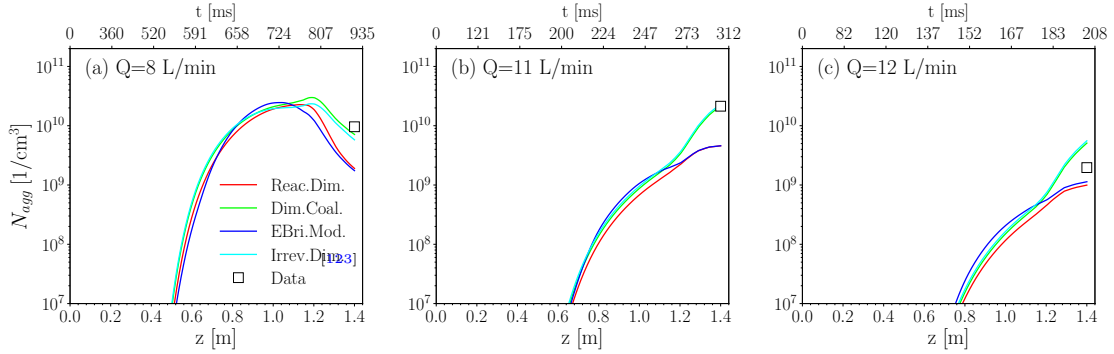


Figure 35: The total number of agglomerates along the PFR for  $Q=8.5$  (a), 11 (b), and 12 L/min (c) obtained using KAUST mechanism and different inception models compared with data [123].

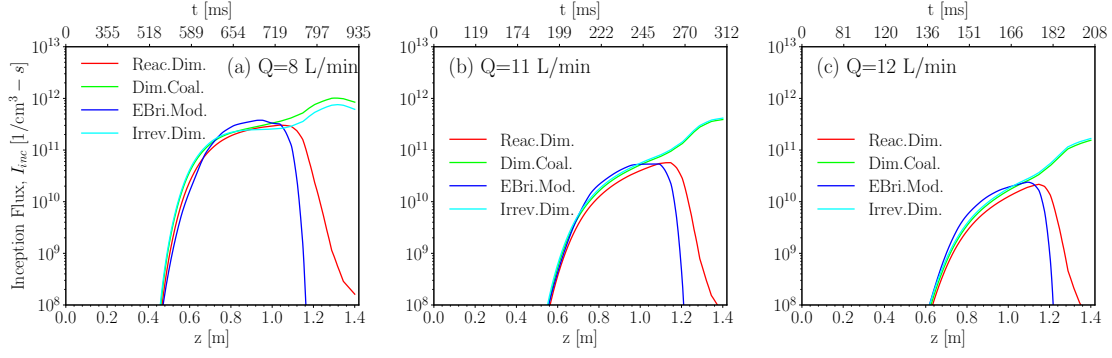


Figure 36: The soot inception flux along the PFR for  $Q=8.5$  (a), 11 (b), and 12 L/min (c) obtained using KAUST mechanism and different inception models.

## 8.4 The effect of particle dynamics model

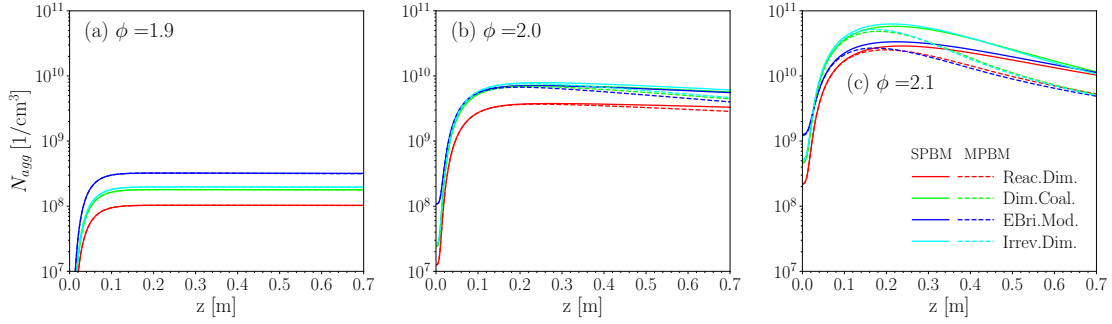


Figure 37: The effect of particle dynamics on total number of agglomerates,  $N_{agg}$  along the PFR in the downstream of a PSR [121] for  $\phi=1.9$  (a), 2.0 (b), and 2.1 (c) obtained using KAUST mechanism and different inception models.

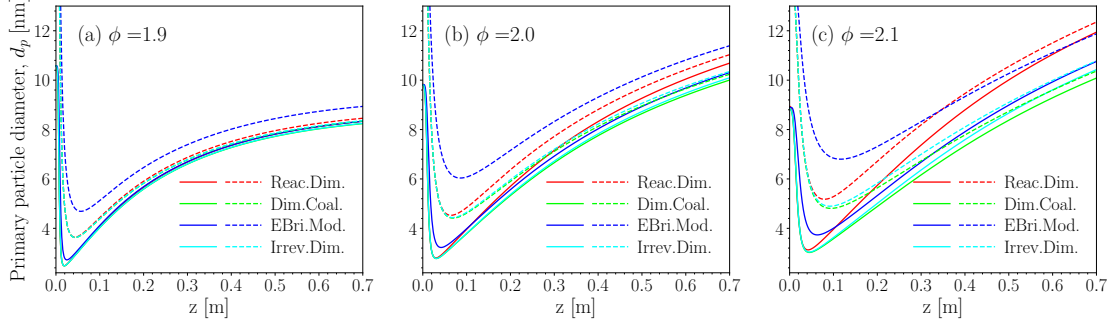


Figure 38: The effect of particle dynamics on primary particle diameter,  $d_p$  along the PFR in the downstream of a PSR [121] for  $\phi=1.9$  (a), 2.0 (b), and 2.1 (c) obtained using KAUST mechanism and different inception models.

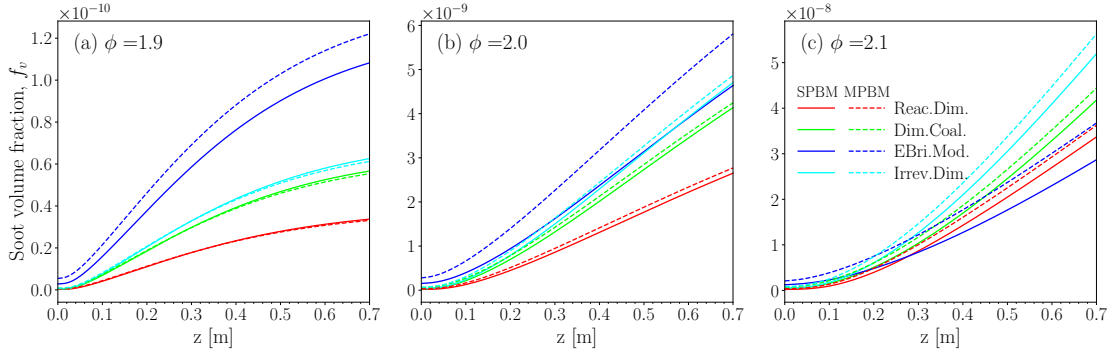


Figure 39: The effect of particle dynamics on soot volume fraction,  $f_v$  along the PFR in the downstream of a PSR [121] for  $\phi=1.9$  (a), 2.0 (b), and 2.1 (c) obtained using KAUST mechanism and different inception models.

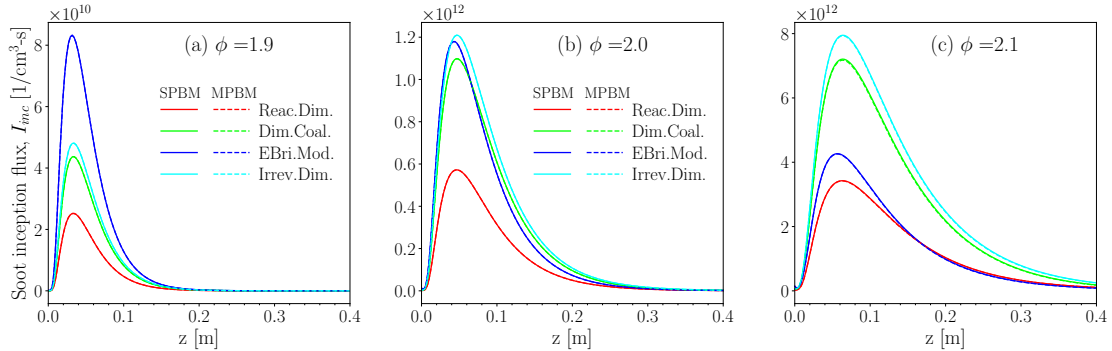


Figure 40: The effect of particle dynamics on soot inception flux,  $I_{inc}$  along the PFR in the downstream of a PSR [121] for  $\phi=1.9$  (a), 2.0 (b), and 2.1 (c) obtained using KAUST mechanism and different inception models.

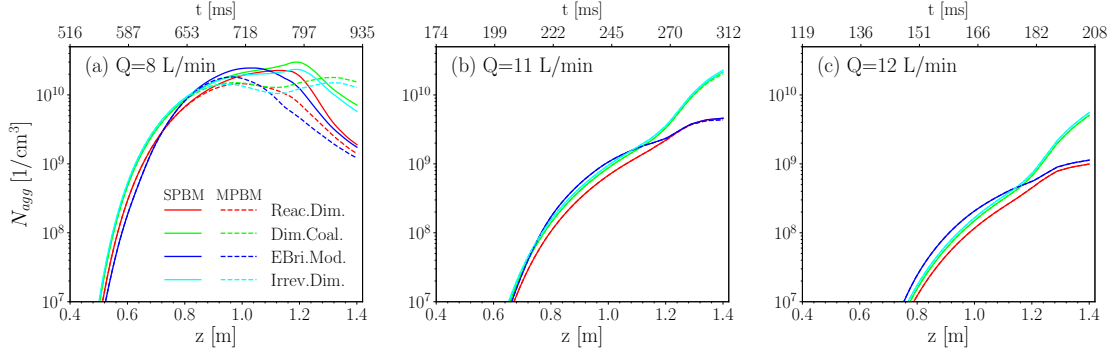


Figure 41: The effect of particle dynamics on total number of agglomerates,  $N_{agg}$  along the PFR for  $Q=8$  (a), 11 (b), and 12 L/min (c) using different inception models.

Fig.41 compares  $N_{agg}$  predicted by the sectional (solid) and monodisperse (dashed) population balance model using different inception models. For  $Q=8$  L/min,  $N_{agg}$  is the same for both particle dynamics model up to 0.8 where soot inception has dominant effect on total number of agglomerates compared to coagulation, but after that monodisperse model predicts stronger collision rate leading to smaller number of agglomerates after the peak. When the monodisperse model is used with Dimer Coalescence and Irreversible Dimerization, the underprediction of  $N_{agg}$  is followed by a secondary increase that exceed the prediction of the sectional model. This behavior can be better understood by looking at inception fluxes shown in Fig. 42 that are the same for both particle dynamics models. These two inception models continue to produce new particles in the cooling region of the reactor near the end due to their weak temperature dependence. This causes a significant increase in  $N_{agg}$  for both particle dynamics models. The peak number concentration of agglomerates is larger for the sectional model resulting in a stronger decay near the end of the reactor.

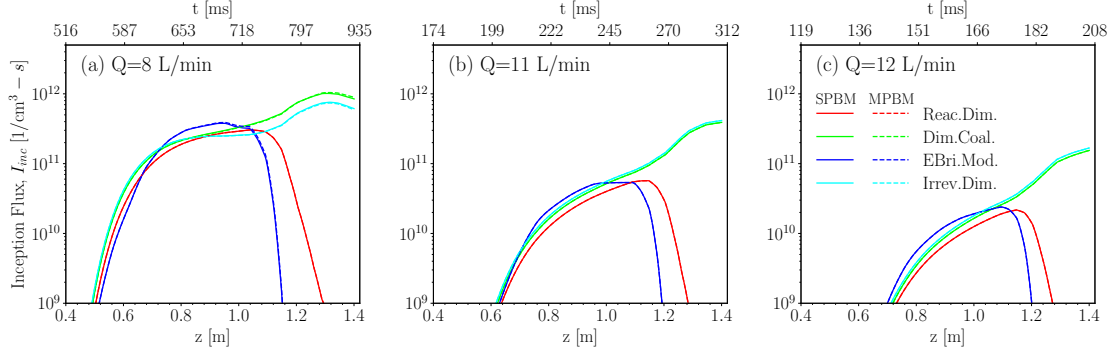


Figure 42: The effect of particle dynamics on inception flux,  $I_{inc}$  along the PFR for  $Q=8.5$  (a), 11 (b), and 12 L/min (c) using different inception models in a 0.6% $C_2H_4$  pyrolysis in a flow reactor [123]

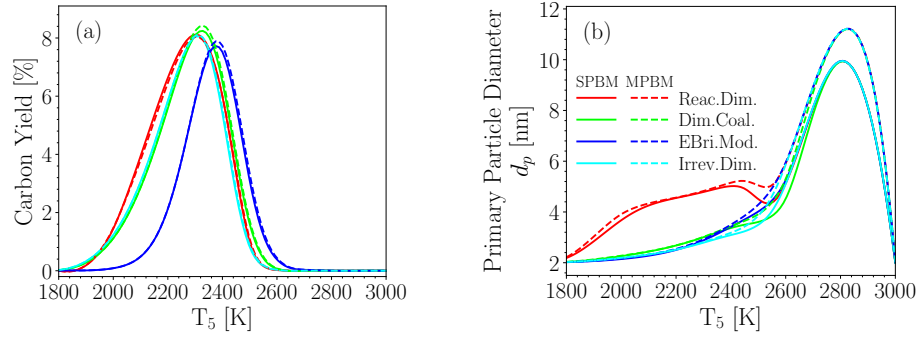


Figure 43: The effect of particle dynamics model on soot carbon yield (a) and mean primary particle diameter,  $d_p$  (b) at  $t=1.5$  ms over  $1800 < T_5 < 3000$  K during 5%CH<sub>4</sub> pyrolysis [118]

### 8.5 The effect of inception flux

### 8.6 The effect of PAH adsorption

## 9 Conclusion



## References

- [1] Andrea D’Anna. Combustion-formed nanoparticles. *Proceedings of the Combustion Institute*, 32(1):593–613, 2009.
- [2] Gunnar Myhre, Drew Shindell, and Julia Pongratz. Anthropogenic and natural radiative forcing. 2014.
- [3] Paul JA Borm, Roel PF Schins, and Catrin Albrecht. Inhaled particles and lung cancer, part b: paradigms and risk assessment. *International journal of cancer*, 110(1):3–14, 2004.
- [4] Rituraj Niranjana and Ashwani Kumar Thakur. The toxicological mechanisms of environmental soot (black carbon) and carbon black: focus on oxidative stress and inflammatory pathways. *Frontiers in immunology*, 8:763, 2017.
- [5] Jennifer L Nichols, Elizabeth Oesterling Owens, Steven J Dutton, and Thomas J Luben. Systematic review of the effects of black carbon on cardiovascular disease among individuals with pre-existing disease. *International Journal of Public Health*, 58:707–724, 2013.
- [6] International Carbon Black Association et al. Carbon black user’s guide. available at [www.carbon-black.org](http://www.carbon-black.org), 2016.
- [7] Verónica Palomares, Aintzane Goñi, Izaskun Gil De Muro, Iratxe De Meatza, Miguel Bengoechea, Igor Cantero, and Teófilo Rojo. Conductive additive content balance in li-ion battery cathodes: Commercial carbon blacks vs. in situ carbon from lifepo4/c composites. *J. Power Sources*, 195:7661–7668, 2010. ISSN 0378-7753.
- [8] Roop Chand Bansal, Meng-Jiao Wang, and JB Donnet. Carbon black. *Science and Technology*, 133, 1993.
- [9] Tianyang Li, Christophe Rehmet, Yan Cheng, Yong Jin, and Yi Cheng. Experimental comparison of methane pyrolysis in thermal plasma. *Plasma Chemistry and Plasma Processing*, 37:1033–1049, 2017.
- [10] Laurent Fulcheri, Vandad-Julien Rohani, Elliott Wyse, Ned Hardman, and Enoch Dames. An energy-efficient plasma methane pyrolysis process for high yields of carbon black and hydrogen. *International Journal of Hydrogen Energy*, 48(8):2920–2928, 2023.
- [11] Shashank Reddy Patlolla, Kyle Katsu, Amir Sharafian, Kevin Wei, Omar E Herrera, and Walter Mérida. A review of methane pyrolysis technologies for hydrogen production. *Renewable and Sustainable Energy Reviews*, 181:113323, 2023.
- [12] Wonihl Cho, Seung-Ho Lee, Woo-Sung Ju, Youngsoo Baek, and Joong Kee Lee. Conversion of natural gas to hydrogen and carbon black by plasma and application of plasma carbon black. *Catalysis Today*, 98(4):633–638, 2004.
- [13] Soo-Jin Park, Min-Kang Seo, and Changwoon Nah. Influence of surface characteristics of carbon blacks on cure and mechanical behaviors of rubber matrix compoundings. *Journal of colloid and interface science*, 291(1):229–235, 2005.
- [14] Ann Y Watson and Peter A Valberg. Carbon black and soot: two different substances. *AIHAJ-American Industrial Hygiene Association*, 62(2):218–228, 2001.
- [15] C Russo, A Tregrossi, and A Ciajolo. Dehydrogenation and growth of soot in premixed flames. *Proceedings of the Combustion Institute*, 35(2):1803–1809, 2015.
- [16] Madhu Singh and Randy L Vander Wal. Nanostructure quantification of carbon blacks. *C*, 5(1):2, 2018.

- [17] Randy L Vander Wal, Aleksey Yezerets, Neal W Currier, Do Heui Kim, and Chong Min Wang. Hrtem study of diesel soot collected from diesel particulate filters. *Carbon*, 45(1):70–77, 2007.
- [18] Magín Lapuerta, Javier Barba, Anton D Sediako, Mohammad Reza Kholghy, and Murray J Thomson. Morphological analysis of soot agglomerates from biodiesel surrogates in a coflow burner. *Journal of Aerosol Science*, 111:65–74, 2017.
- [19] Kiminori Ono, Kazuki Dewa, Yoshiya Matsukawa, Yasuhiro Saito, Yohsuke Matsushita, Hideyuki Aoki, Koki Era, Takayuki Aoki, and Togo Yamaguchi. Experimental evidence for the sintering of primary soot particles. *Journal of Aerosol Science*, 105:1–9, 2017.
- [20] Jiangjun Wei, Yang Zeng, Mingzhang Pan, Yuan Zhuang, Liang Qiu, Taotao Zhou, and Yongqiang Liu. Morphology analysis of soot particles from a modern diesel engine fueled with different types of oxygenated fuels. *Fuel*, 267:117248, 2020.
- [21] M Alfè, B Apicella, Rouzaud Barbella, J-N Rouzaud, A Tregrossi, and A Ciajolo. Structure–property relationship in nanostructures of young and mature soot in premixed flames. *Proceedings of the Combustion Institute*, 32(1):697–704, 2009.
- [22] Stephen E Stein and A Fahr. High-temperature stabilities of hydrocarbons. *The Journal of Physical Chemistry*, 89(17):3714–3725, 1985.
- [23] Hai Wang. Formation of nascent soot and other condensed-phase materials in flames. *Proc Combust Inst.*, 33:41–67, 2011. ISSN 15407489.
- [24] Michael Frenklach. Reaction mechanism of soot formation in flames. *Physical chemistry chemical Physics*, 4(11):2028–2037, 2002.
- [25] Jennifer D Herdman and J Houston Miller. Intermolecular potential calculations for polynuclear aromatic hydrocarbon clusters. *The Journal of Physical Chemistry A*, 112(28):6249–6256, 2008.
- [26] Tim S Totton, Alston J Misquitta, and Markus Kraft. A quantitative study of the clustering of polycyclic aromatic hydrocarbons at high temperatures. *Physical chemistry chemical physics*, 14(12):4081–4094, 2012.
- [27] Michael Frenklach and Hai Wang. Detailed modeling of soot particle nucleation and growth. In *Symposium (International) on Combustion*, volume 23, pages 1559–1566. Elsevier, 1991.
- [28] Steffen Salenbauch, Alberto Cuoci, Alessio Frassoldati, Chiara Saggese, Tiziano Faravelli, and Christian Hasse. Modeling soot formation in premixed flames using an extended conditional quadrature method of moments. *Combustion and Flame*, 162(6):2529–2543, 2015.
- [29] Pascale Desgroux, Alessandro Faccinetto, Xavier Mercier, Thomas Mouton, Damien Aubagnac Karkar, and Abderrahman El Bakali. Comparative study of the soot formation process in a “nucleation” and a “sooting” low pressure premixed methane flame. *Combustion and Flame*, 184:153–166, 2017.
- [30] Yu Wang, Abhijeet Raj, and Suk Ho Chung. Soot modeling of counterflow diffusion flames of ethylene-based binary mixture fuels. *Combustion and Flame*, 162(3):586–596, 2015.
- [31] Lei Xu, Fuwu Yan, Mengxiang Zhou, and Yu Wang. An experimental and modeling study on sooting characteristics of laminar counterflow diffusion flames with partial premixing. *Energy*, 218:119479, 2021.
- [32] Mohammad Reza Kholghy, Armin Veshkini, and Murray John Thomson. The core–shell internal nanostructure of soot—a criterion to model soot maturity. *Carbon*, 100:508–536, 2016.

- [33] Armin Veshkini, Seth B Dworkin, and Murray J Thomson. Understanding soot particle size evolution in laminar ethylene/air diffusion flames using novel soot coalescence models. *Combustion Theory and Modelling*, 20(4):707–734, 2016.
- [34] J Houston Miller, Kermit C Smyth, and W Gary Mallard. Calculations of the dimerization of aromatic hydrocarbons: Implications for soot formation. In *Symposium (International) on Combustion*, volume 20, pages 1139–1147. Elsevier, 1985.
- [35] Hassan Sabbah, Ludovic Biennier, Stephen J Klippenstein, Ian R Sims, and Bertrand R Rowe. Exploring the role of pahs in the formation of soot: Pyrene dimerization. *The Journal of Physical Chemistry Letters*, 1(19):2962–2967, 2010.
- [36] Ali Naseri, M Reza Kholghy, Neil A Juan, and Murray J Thomson. Simulating yield and morphology of carbonaceous nanoparticles during fuel pyrolysis in laminar flow reactors enabled by reactive inception and aromatic adsorption. *Combustion and Flame*, 237:111721, 2022.
- [37] Nazly E Sanchez, Alicia Callejas, Angela Millera, Rafael Bilbao, and Maria U Alzueta. Polycyclic aromatic hydrocarbon (pah) and soot formation in the pyrolysis of acetylene and ethylene: effect of the reaction temperature. *Energy & fuels*, 26(8):4823–4829, 2012.
- [38] Sanghwan Cho, Seunghoon Lee, Wonnam Lee, and Sunho Park. Synthesis of primary-particle-size-tuned soot particles by controlled pyrolysis of hydrocarbon fuels. *Energy & Fuels*, 30(8):6614–6619, 2016.
- [39] Meghdad Saffaripour, Armin Veshkini, Mohammadreza Kholghy, and Murray J Thomson. Experimental investigation and detailed modeling of soot aggregate formation and size distribution in laminar coflow diffusion flames of jet a-1, a synthetic kerosene, and n-decane. *Combustion and Flame*, 161(3):848–863, 2014.
- [40] J Houston Miller. The kinetics of polynuclear aromatic hydrocarbon agglomeration in flames. In *Symposium (International) on Combustion*, volume 23, pages 91–98. Elsevier, 1991.
- [41] Anna Giordana, Andrea Maranzana, and Glaucio Tonachini. Theoretical investigation of soot nanoparticle inception via polycyclic aromatic hydrocarbon coagulation (condensation): Energetic, structural, and electronic features. *The Journal of Physical Chemistry C*, 115(5):1732–1739, 2011.
- [42] NA Eaves, SB Dworkin, and MJ Thomson. The importance of reversibility in modeling soot nucleation and condensation processes. *Proceedings of the Combustion Institute*, 35(2):1787–1794, 2015.
- [43] Mohammad Reza Kholghy, Nick Anthony Eaves, Armin Veshkini, and Murray John Thomson. The role of reactive pah dimerization in reducing soot nucleation reversibility. *Proceedings of the Combustion Institute*, 37(1):1003–1011, 2019.
- [44] Mohammad R Kholghy, Georgios A Kelesidis, and Sotiris E Pratsinis. Reactive polycyclic aromatic hydrocarbon dimerization drives soot nucleation. *Physical Chemistry Chemical Physics*, 20(16):10926–10938, 2018.
- [45] Michael Frenklach and Alexander M Mebel. On the mechanism of soot nucleation. *Physical Chemistry Chemical Physics*, 22(9):5314–5331, 2020.
- [46] Aamir D Abid, Joaquin Camacho, David A Sheen, and Hai Wang. Quantitative measurement of soot particle size distribution in premixed flames—the burner-stabilized stagnation flame approach. *Combustion and Flame*, 156(10):1862–1870, 2009.
- [47] Jörg Appel, Henning Bockhorn, and Michael Frenklach. Kinetic modeling of soot formation with detailed chemistry and physics: laminar premixed flames of c2 hydrocarbons. *Combustion and flame*, 121(1-2):122–136, 2000.

- [48] IT Woods and BS Haynes. Soot surface growth at active sites. *Combustion and flame*, 85 (3-4):523–525, 1991.
- [49] Cameron J Dasch. The decay of soot surface growth reactivity and its importance in total soot formation. *Combustion and flame*, 61(3):219–225, 1985.
- [50] Hope A Michelsen, Meredith B Colket, Per-Erik Bengtsson, Andrea D’anna, Pascale Desgroux, Brian S Haynes, J Houston Miller, Graham J Nathan, Heinz Pitsch, and Hai Wang. A review of terminology used to describe soot formation and evolution under combustion and pyrolytic conditions. *ACS nano*, 14(10):12470–12490, 2020.
- [51] OI Obolensky, VV Semenikhina, AV Solov’Yov, and W Greiner. Interplay of electrostatic and van der waals forces in coronene dimer. *International Journal of Quantum Chemistry*, 107(6): 1335–1343, 2007.
- [52] Eirini Goudeli, Maximilian L Eggersdorfer, and Sotiris E Pratsinis. Coagulation of agglomerates consisting of polydisperse primary particles. *Langmuir*, 32:9276–9285, 2016. ISSN 0743-7463.
- [53] FS Lai, SK Friedlander, J Pich, and GM Hidy. The self-preserving particle size distribution for brownian coagulation in the free-molecule regime. *Journal of Colloid and Interface Science*, 39(2):395–405, 1972.
- [54] Raymond D Mountain, George W Mulholland, and Howard Baum. Simulation of aerosol agglomeration in the free molecular and continuum flow regimes. *Journal of Colloid and Interface Science*, 114(1):67–81, 1986.
- [55] Georgios A. Kelesidis, Eirini Goudeli, and Sotiris E. Pratsinis. Morphology and mobility diameter of carbonaceous aerosols during agglomeration and surface growth. *Carbon*, 121: 527–535, 9 2017. ISSN 00086223.
- [56] Georgios A Kelesidis and Eirini Goudeli. Self-preserving size distribution and collision frequency of flame-made nanoparticles in the transition regime. *Proceedings of the Combustion Institute*, 38(1):1233–1240, 2021.
- [57] Georgios A. Kelesidis, Eirini Goudeli, and Sotiris E. Pratsinis. Flame synthesis of functional nanostructured materials and devices: Surface growth and aggregation. *Proc Combust Inst* ., 36:29–50, 2017. ISSN 15407489.
- [58] Georgios A Kelesidis and Sotiris E Pratsinis. A perspective on gas-phase synthesis of nano-materials: Process design, impact and outlook. *Chemical Engineering Journal*, 421:129884, 2021.
- [59] Yun Xiong and Sotiris E Pratsinis. Formation of agglomerate particles by coagulation and sintering—part i. a two-dimensional solution of the population balance equation. *J. Aerosol Sci.*, 24:283–300, 1993. ISSN 0021-8502.
- [60] SH Park, SN Rogak, WK Bushe, JZ Wen, and MJ Thomson. An aerosol model to predict size and structure of soot particles. *Combustion Theory and Modelling*, 9(3):499–513, 2005.
- [61] MA Schiener and RP Lindstedt. Transported probability density function based modelling of soot particle size distributions in non-premixed turbulent jet flames. *Proceedings of the Combustion Institute*, 37(1):1049–1056, 2019.
- [62] Themis Matsoukas and Sheldon K Friedlander. Dynamics of aerosol agglomerate formation. *Journal of Colloid and Interface Science*, 146(2):495–506, 1991.
- [63] NA Fuchs. The mechanics of aerosol pergamon. *New York*, 1964.

- [64] Yun Xiong and Sotiris E Pratsinis. Formation of agglomerate particles by coagulation and sintering—part i. a two-dimensional solution of the population balance equation. *Journal of Aerosol Science*, 24(3):283–300, 1993.
- [65] MD Smooke, MB Long, BC Connelly, MB Colket, and RJ Hall. Soot formation in laminar diffusion flames. *Combustion and Flame*, 143(4):613–628, 2005.
- [66] Damien Aubagnac-Karkar, Abderrahman El Bakali, and Pascale Desgroux. Soot particles inception and pah condensation modelling applied in a soot model utilizing a sectional method. *Combustion and Flame*, 189:190–206, 2018.
- [67] Andrei Kazakov and Michael Frenklach. Dynamic modeling of soot particle coagulation and aggregation: Implementation with the method of moments and application to high-pressure laminar premixed flames. *Combustion and flame*, 114(3-4):484–501, 1998.
- [68] F Einar Kruis, Karl A Kusters, Sotiris E Pratsinis, and Brian Scarlett. A simple model for the evolution of the characteristics of aggregate particles undergoing coagulation and sintering. *Aerosol science and technology*, 19(4):514–526, 1993.
- [69] Patrick T Spicer, Olivier Chaoul, Stavros Tsantilis, and Sotiris E Pratsinis. Titania formation by ticl<sub>4</sub> gas phase oxidation, surface growth and coagulation. *J. Aerosol Sci.*, 33:17–34, 2002. ISSN 0021-8502.
- [70] Georgios A Kelesidis and Sotiris E Pratsinis. Estimating the internal and surface oxidation of soot agglomerates. *Combustion and Flame*, 209:493–499, 2019.
- [71] Aamir D Abid, Nicholas Heinz, Erik D Tolmachoff, Denis J Phares, Charles S Campbell, and Hai Wang. On evolution of particle size distribution functions of incipient soot in premixed ethylene-oxygen-argon flames. *Combustion and Flame*, 154(4):775–788, 2008.
- [72] X Ma, CD Zangmeister, and MR Zachariah. Soot oxidation kinetics: a comparison study of two tandem ion-mobility methods. *The Journal of Physical Chemistry C*, 117(20):10723–10729, 2013.
- [73] Joaquin Camacho, Changran Liu, Chen Gu, He Lin, Zhen Huang, Quanxi Tang, Xiaoqing You, Chiara Sagge, Yang Li, Heejung Jung, et al. Mobility size and mass of nascent soot particles in a benchmark premixed ethylene flame. *Combustion and Flame*, 162(10):3810–3822, 2015.
- [74] Arto J Gröhn, Sotiris E Pratsinis, and Karsten Wegner. Fluid-particle dynamics during combustion spray aerosol synthesis of zro<sub>2</sub>. *Chemical Engineering Journal*, 191:491–502, 2012.
- [75] Sotiris E Pratsinis. Simultaneous nucleation, condensation, and coagulation in aerosol reactors. *Journal of colloid and interface science*, 124(2):416–427, 1988.
- [76] Guillaume Blanquart and Heinz Pitsch. A joint volume-surface-hydrogen multi-variate model for soot formation. *Combustion generated fine carbonaceous particles*, pages 437–463, 2009.
- [77] G Blanquart and H Pitsch. Analyzing the effects of temperature on soot formation with a joint volume-surface-hydrogen model. *Combustion and Flame*, 156(8):1614–1626, 2009.
- [78] Kyo-Seon Kim and Sotiris E Pratsinis. Manufacture of optical waveguide preforms by modified chemical vapor deposition. *AIChE journal*, 34(6):912–921, 1988.
- [79] Michael Frenklach and Stephen J Harris. Aerosol dynamics modeling using the method of moments. *Journal of colloid and interface science*, 118(1):252–261, 1987.
- [80] Stavros Tsantilis and Sotiris E Pratsinis. Soft-and hard-agglomerate aerosols made at high temperatures. *Langmuir*, 20(14):5933–5939, 2004.

- [81] Peter R Lindstedt. Simplified soot nucleation and surface growth steps for non-premixed flames. In *Soot formation in combustion: mechanisms and models*, pages 417–441. Springer, 1994.
- [82] Robert N Grass, Stavros Tsantilis, and Sotiris E Pratsinis. Design of high-temperature, gas-phase synthesis of hard or soft tio<sub>2</sub> agglomerates. *AIChE Journal*, 52(4):1318–1325, 2006.
- [83] David G. Goodwin, Harry K. Moffat, Ingmar Schoegl, Raymond L. Speth, and Bryan W. Weber. Cantera: An object-oriented software toolkit for chemical kinetics, thermodynamics, and transport processes. <https://www.cantera.org>, 2022. Version 2.6.0.
- [84] Hope A Michelsen. Effects of maturity and temperature on soot density and specific heat. *Proceedings of the Combustion Institute*, 38(1):1197–1205, 2021.
- [85] Kirk A Jensen, Jill M Suo-Anttila, and Linda G Blevins. Measurement of soot morphology, chemistry, and optical properties in the visible and near-infrared spectrum in the flame zone and overfire region of large jp-8 pool fires. *Combustion science and technology*, 179(12):2453–2487, 2007.
- [86] Bonnie J McBride. *Coefficients for calculating thermodynamic and transport properties of individual species*, volume 4513. National Aeronautics and Space Administration, Office of Management . . . , 1993.
- [87] Robert J Kee, Michael E Coltrin, Peter Glarborg, and Huayang Zhu. *Chemically reacting flow: theory, modeling, and simulation*. John Wiley & Sons, 2017.
- [88] Skjalg E Haaland. Simple and explicit formulas for the friction factor in turbulent pipe flow. 1983.
- [89] FP Berger and K-FF-L Hau. Mass transfer in turbulent pipe flow measured by the electrochemical method. *International Journal of Heat and Mass Transfer*, 20(11):1185–1194, 1977.
- [90] George W Mulholland, RJ Samson, RD Mountain, and MH Ernst. Cluster size distribution for free molecular agglomeration. *Energy & Fuels*, 2(4):481–486, 1988.
- [91] RC Ball and R Jullien. Finite size effects in cluster-cluster aggregation. *Journal de Physique Lettres*, 45(21):1031–1035, 1984.
- [92] Jérôme Yon, A Bescond, and F-X Ouf. A simple semi-empirical model for effective density measurements of fractal aggregates. *Journal of Aerosol Science*, 87:28–37, 2015.
- [93] Jenny Rissler, Maria E Messing, Azhar I Malik, Patrik T Nilsson, Erik Z Nordin, Mats Bohgard, Mehri Sanati, and Joakim H Pagels. Effective density characterization of soot agglomerates from various sources and comparison to aggregation theory. *Aerosol Science and Technology*, 47(7):792–805, 2013.
- [94] Ganesan Narsimhan and Eli Ruckenstein. The brownian coagulation of aerosols over the entire range of knudsen numbers: Connection between the sticking probability and the interaction forces. *Journal of colloid and interface science*, 104(2):344–369, 1985.
- [95] Antonio D’Alessio, AC Barone, R Cau, Andrea D’Anna, and P Minutolo. Surface deposition and coagulation efficiency of combustion generated nanoparticles in the size range from 1 to 10 nm. *Proceedings of the Combustion Institute*, 30(2):2595–2603, 2005.
- [96] Hwa-Chi Wang and Gerhard Kasper. Filtration efficiency of nanometer-size aerosol particles. *Journal of Aerosol Science*, 22(1):31–41, 1991.
- [97] Dingyu Hou, Diyuan Zong, Casper S Lindberg, Markus Kraft, and Xiaoqing You. On the coagulation efficiency of carbonaceous nanoparticles. *Journal of Aerosol Science*, 140:105478, 2020.

- [98] Anna Ciajolo, Rosalba Barbella, Antonio Tregrossi, and Loretta Bonfanti. Spectroscopic and compositional signatures of pah-loaded mixtures in the soot inception region of a premixed ethylene flame. In *Symposium (International) on Combustion*, volume 27, pages 1481–1487. Elsevier, 1998.
- [99] Christopher Betrancourt, Fengshan Liu, Pascale Desgroux, Xavier Mercier, Alessandro Facinetto, Maurin Salamanca, Lena Ruwe, Katharina Kohse-Höinghaus, Daniel Emmrich, André Beyer, et al. Investigation of the size of the incandescent incipient soot particles in premixed sooting and nucleation flames of n-butane using lii, him, and 1 nm-smgs. *Aerosol Science and Technology*, 51(8):916–935, 2017.
- [100] Hope A Michelsen. Probing soot formation, chemical and physical evolution, and oxidation: A review of in situ diagnostic techniques and needs. *Proceedings of the Combustion Institute*, 36(1):717–735, 2017.
- [101] Nikolaj A Fuchs, RE Daisley, Marina Fuchs, CN Davies, and ME Straumanis. The mechanics of aerosols, 1965.
- [102] Jin Jwang Wu and Richard C Flagan. A discrete-sectional solution to the aerosol dynamic equation. *Journal of Colloid and interface Science*, 123(2):339–352, 1988.
- [103] BS Haynes and H Gg Wagner. The surface growth phenomenon in soot formation. *Zeitschrift für Physikalische Chemie*, 133(2):201–213, 1982.
- [104] Stephen J Harris and Anita M Weiner. Chemical kinetics of soot particle growth. *Annual Review of Physical Chemistry*, 36(1):31–52, 1985.
- [105] KH Homann. Formation of large molecules, particulates and ions in premixed hydrocarbon flames; progress and unresolved questions. In *Symposium (International) on Combustion*, volume 20, pages 857–870. Elsevier, 1985.
- [106] Armin Veshkini. *Understanding Soot Particle Growth Chemistry and Particle Sizing Using a Novel Soot Growth and Formation Model*. University of Toronto (Canada), 2015.
- [107] Bin Zhao, Zhiwei Yang, Murray V Johnston, Hai Wang, Anthony S Wexler, Michael Balthasar, and Markus Kraft. Measurement and numerical simulation of soot particle size distribution functions in a laminar premixed ethylene-oxygen-argon flame. *Combustion and Flame*, 133(1-2):173–188, 2003.
- [108] Joachim Happold, Horst-Henning Grotheer, and Manfred Aigner. Soot precursors consisting of stacked pericondensed pahs. *Combustion generated fine carbonaceous particles*, pages 275–285, 2009.
- [109] K Olof Johansson, Tyler Dillstrom, Matteo Monti, Farid El Gabaly, Matthew F Campbell, Paul E Schrader, Denisia M Popolan-Vaida, Nicole K Richards-Henderson, Kevin R Wilson, Angela Violi, et al. Formation and emission of large furans and oxygenated hydrocarbons from flames. *Proceedings of the National Academy of Sciences*, 113(30):8374–8379, 2016.
- [110] J Houston Miller, W Gary Mallard, and Kermit C Smyth. Intermolecular potential calculations for polycyclic aromatic hydrocarbons. *The Journal of Physical Chemistry*, 88(21):4963–4970, 1984.
- [111] Yoichiro Araki, Yoshiya Matsukawa, Yasuhiro Saito, Yohsuke Matsushita, Hideyuki Aoki, Koki Era, and Takayuki Aoki. Effects of carrier gas on the properties of soot produced by ethylene pyrolysis. *Fuel Processing Technology*, 213:106673, 2021.
- [112] Binxuan Sun, Stelios Rigopoulos, and Anxiong Liu. Modelling of soot coalescence and aggregation with a two-population balance equation model and a conservative finite volume method. *Combustion and Flame*, 229:111382, 2021.

- [113] A Tregrossi, A Ciajolo, and R Barbella. The combustion of benzene in rich premixed flames at atmospheric pressure. *Combustion and flame*, 117(3):553–561, 1999.
- [114] Eirini Goudeli, Maximilian L Eggersdorfer, and Sotiris E Pratsinis. Coagulation–agglomeration of fractal-like particles: Structure and self-preserving size distribution. *Langmuir*, 31(4):1320–1327, 2015.
- [115] M Reza Kholghy and Georgios A Kelesidis. Surface growth, coagulation and oxidation of soot by a monodisperse population balance model. *Combustion and Flame*, 227:456–463, 2021.
- [116] Srinivas Vemury and Sotiris E Pratsinis. Self-preserving size distributions of agglomerates. *Journal of Aerosol Science*, 26(2):175–185, 1995.
- [117] Scott Stouffer, Richard Striebich, Joseph Zelina, and Charles Frayne. Combustion particulates mitigation investigation using a well-stirred reactor. In *38th AIAA/ASME/SAE/ASEE Joint Propulsion Conference & Exhibit*, page 3723, 2002.
- [118] GL Agafonov, IV Biler, PA Vlasov, IV Zhil’tsova, Yu A Kolbanovskii, VN Smirnov, and AM Tereza. Unified kinetic model of soot formation in the pyrolysis and oxidation of aliphatic and aromatic hydrocarbons in shock waves. *Kinetics and Catalysis*, 57:557–572, 2016.
- [119] SC Lee and CL Tien. Optical constants of soot in hydrocarbon flames. In *Symposium (international) on combustion*, volume 18, pages 1159–1166. Elsevier, 1981.
- [120] GL Agafonov, PA Vlasov, and VN Smirnov. Soot formation in the pyrolysis of benzene, methylbenzene, and ethylbenzene in shock waves. *Kinetics and Catalysis*, 52:358–370, 2011.
- [121] Samuel L Manzello, David B Lenhert, Ahmet Yozgatligil, Michael T Donovan, George W Mulholland, Michael R Zachariah, and Wing Tsang. Soot particle size distributions in a well-stirred reactor/plug flow reactor. *Proceedings of the Combustion Institute*, 31(1):675–683, 2007.
- [122] David B Lenhert and Samuel L Manzello. Effects of benzene and naphthalene addition on soot inception in a well-stirred reactor/plug flow reactor. *Proceedings of the Combustion Institute*, 32(1):657–664, 2009.
- [123] Junyu Mei, Mengda Wang, Xiaoqing You, and Chung K Law. Quantitative measurement of particle size distributions of carbonaceous nanoparticles during ethylene pyrolysis in a laminar flow reactor. *Combustion and Flame*, 200:15–22, 2019.